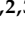




Article

# Geochemistry and Mineralogy of Rare Earth Elements (REE) in Bauxitic Ores of the Catalan Coastal Range, NE Spain

Nils Reinhardt <sup>1,2,3,\*</sup>, Joaquín A. Proenza <sup>2</sup> , Cristina Villanova-de-Benavent <sup>2,4</sup>, Thomas Aiglsperger <sup>2,5</sup> , Telm Bover-Arnal <sup>2</sup>, Lisard Torró <sup>2,6</sup> , Ramon Salas <sup>2</sup> and Annika Dziggel <sup>3</sup>

<sup>1</sup> Institute of Mineralogy, Technische Universität Bergakademie Freiberg, Brennhausgasse 14, 09599 Freiberg, Germany

<sup>2</sup> Departament de Mineralogia, Petrologia i Geologia Aplicada, Facultat de Ciències de la Terra, Universitat de Barcelona (UB), Martí i Franquès s/n, 08028 Barcelona, Spain; japroenza@ub.edu (J.A.P.); c.villanova-de-benavent@brighton.ac.uk (C.V.-d.-B.); thomas.aiglsperger@ltu.se (T.A.); telm.boverarnal@ub.edu (T.B.-A.); lisardtorro@hotmail.com (L.T.); ramonsalas@ub.edu (R.S.)

<sup>3</sup> Institute of Applied Mineralogy and Economic Geology (IML), RWTH Aachen University, Wüllnerstraße 2, 52062 Aachen, Germany; adziggel@emr.rwth-aachen.de

<sup>4</sup> School of Environment and Technology (SET), University of Brighton, Cockcroft Building, Lewes Road, Brighton BN4 2GI, UK

<sup>5</sup> Department of Civil Engineering and Natural Resources, Division of Geosciences and Environmental Engineering, Luleå University of Technology, SE 97187 Luleå, Sweden

<sup>6</sup> Especialidad Ingeniería Geológica, Sección Ingeniería de Minas, Pontificia Universidad Católica del Perú, Av. Universitaria 1801, San Miguel, Lima 15088, Peru

\* Correspondence: nils.reinhardt@mineral.tu-freiberg.de; Tel.: +49-3731-393398

Received: 8 October 2018; Accepted: 27 November 2018; Published: 1 December 2018



**Abstract:** Karst bauxite deposits are currently investigated as a new resource for rare earth elements (REE) in order to avoid present and future supply shortfalls of these critical metals. The present work focuses on the geochemistry and mineralogy of the REE in karst bauxite deposits of the Catalan Coastal Range (CCR), NE-Spain. It is revealed that the studied bauxitic ores have a dominant breccia and local ooido-pisoidic and pelitomorph texture. The bauxitic ores are mostly composed of kaolinite and hematite, as well as of lesser amounts of boehmite, diaspore, rutile and calcite. The mineralogy and major element composition indicate incomplete bauxitization of an argillaceous precursor material possibly derived from the erosion of the Mesozoic Ebro massif paleo-high. The studied bauxites are characterized by  $\Sigma$ REE (including Sc, Y) between 286 and 820 ppm (av. 483 ppm) and light REE to heavy REE (LREE/HREE) ratios up to 10.6. REE are mainly concentrated in phosphate minerals, identified as monazite-(Ce) and xenotime-(Y) of detrital origin and unidentified REE-phosphates of a possible authigenic origin. REE remobilization presumably took place under acidic conditions, whereas REE entrapment in the form of precipitation of authigenic rare earth minerals from percolating solutions was related to neutral to slightly alkaline conditions. During the bauxitization process no significant REE fractionation took place and the REE distribution pattern of the bauxitic ores was governed by the REE budget of the precursor material. Finally, adsorption as a main REE scavenging mechanism in the studied CCR bauxite deposits should not be considered, since the presented data did not reveal significant REE contents in Fe- and Mn-oxyhydroxides and clay minerals.

**Keywords:** karst bauxite; rare earth elements; monazite; xenotime; geochemistry; mineralogy; Catalonia; Spain

## 1. Introduction

According to the International Union of Pure and Applied Chemistry (IUPAC) REE are a group of 17 elements with a similar geochemical behavior comprising the lanthanides, yttrium (Y) and scandium (Sc) [1]. Most earth scientists, however, traditionally exclude Sc or both Sc and Y and group REE into LREE (La-Eu) and HREE (Gd-Lu) based on their atomic weight [2] and their continuously decreasing atomic radii from La to Lu, a phenomenon called lanthanide contraction [3].

Technological developments have dramatically increased the use of REE in the defense, aerospace, medical and automotive industries. Among others, they are essential components of catalysts, high-strength magnets (mainly NdFeB), super-alloys, display technology and lasers [1,4–7]. Achieving an undistorted and sustainable access to REE is of increasing concern not only in Europe, but also across the globe. The European Commission has indeed categorized these elements as critical raw materials, because of their high economic importance coupled to possible supply shortfalls [8] partly caused by a monopolization of the supply chain by China [4].

REE concentration has been proven to occur in a wide range of geological settings [2,9], including the formation of residual deposits, such as karst bauxites (i.e., bauxites overlying carbonate rocks) [10–13]. Bauxite ore is the primary source of aluminum. Its beneficiation (Al extraction by means of the Bayer process) results in the production of Al and waste material (i.e., bauxite metallurgical residue, the so-called “red mud” [14]). In fact, Deady et al. [15] emphasized that karst bauxite ores are the ideal source material for REE-enriched red mud as the conditions during formation of the bauxite allow for the retention of REE (see also [16–18]).

During laterization and bauxitization processes, intense weathering and the limited mobility of REE in the weathering profiles cause the enrichment of these elements in residual ores, including bauxite, relative to their parent rocks in the form of: (i) concentration of primary (magmatic) refractory REE phases, (ii) precipitation of secondary authigenic/ diagenetic REE phases, (iii) LREE-actinide oxides sorbed in supergene/ epigenetic Fe-oxides and (iv) ion-adsorption clays [13,15,19–21].

In karst bauxites, the most common REE-bearing minerals include fluorocarbonates (bastnäsite-group), phosphates (e.g., monazite-, xenotime-, apatite-groups) and REE-oxides (e.g., cerianite) (e.g., [13,21–25]).

In spite of the growing interest in karst bauxite deposits as potential non-conventional REE resources, data for European karst bauxite deposits, with the exception of Greece [21,26–28], generally are scarce (e.g., Italy [29–33], Turkey [34], Hungary [22] or Montenegro [20,35]). Karst bauxite deposits in Spain belong to the Mediterranean bauxite belt and are located in four bauxite regions: (i) The Subbetic Zone in the Betic Cordillera, (ii) the Linking Zone (LZ) between the CCR and the Iberian Range, (iii) the CCR and (iv) the Pyrenean System [36]. Salas et al. [37] used REE distribution patterns to infer on the parental material of karst bauxite deposits of the LZ and the CCR. They concluded that bauxites were probably derived from lower Barremian laterized clays of the Cantaperdius formation situated some 12 to 15 km to the N. Ordóñez et al. [38] studied the geochemistry of karst bauxite deposits of the LZ, the CCR and the southern Pyrenees, describing  $\Sigma$ REE of up to 689.7 ppm. These authors stressed that  $\Sigma$ REE values did not correlate with the major element contents. More recently, Yuste et al. [39,40] published data on the geochemistry of the Fuentespalda karst bauxite deposit (Teruel) in the LZ, reporting  $\Sigma$ REE values of up to 815.75 ppm. However, accurate data on REE-bearing mineral phases in Spanish karst bauxite deposits are scarce so far. Therefore, we aim to provide new data on the REE geochemistry and mineralogy of bauxite ores of the CCR, NE-Spain by means of a thorough petrographic and geochemical characterization, including the investigation of bauxite heavy mineral concentrates. These results, along with mineralogical and geochemical data are used to constrain the origin of the bauxite ores in the study area. It should be highlighted that, to our best knowledge, no detailed mineralogical description of REE-phases in Spanish bauxites exists. Moreover, this work is the first in which hydroseparation techniques have been applied for the study of Spanish bauxites.

## 2. Geological Setting

Three mountain chains associated with the Alpine Orogeny dominate the NE part of the Iberian Peninsula: The Pyrenees, the Iberian Chain (IC) and the CCR. During the Cenozoic, the Ebro Basin developed as the foreland basin of the afore-mentioned mountain chains (Figure 1). Dominant tectonic structures trend NW-SE in the IC, whereas they trend NE-SW in the CCR. The LZ, which is characterized by dominant E-W trending tectonic structures, is located between the IC and the CCR [41].

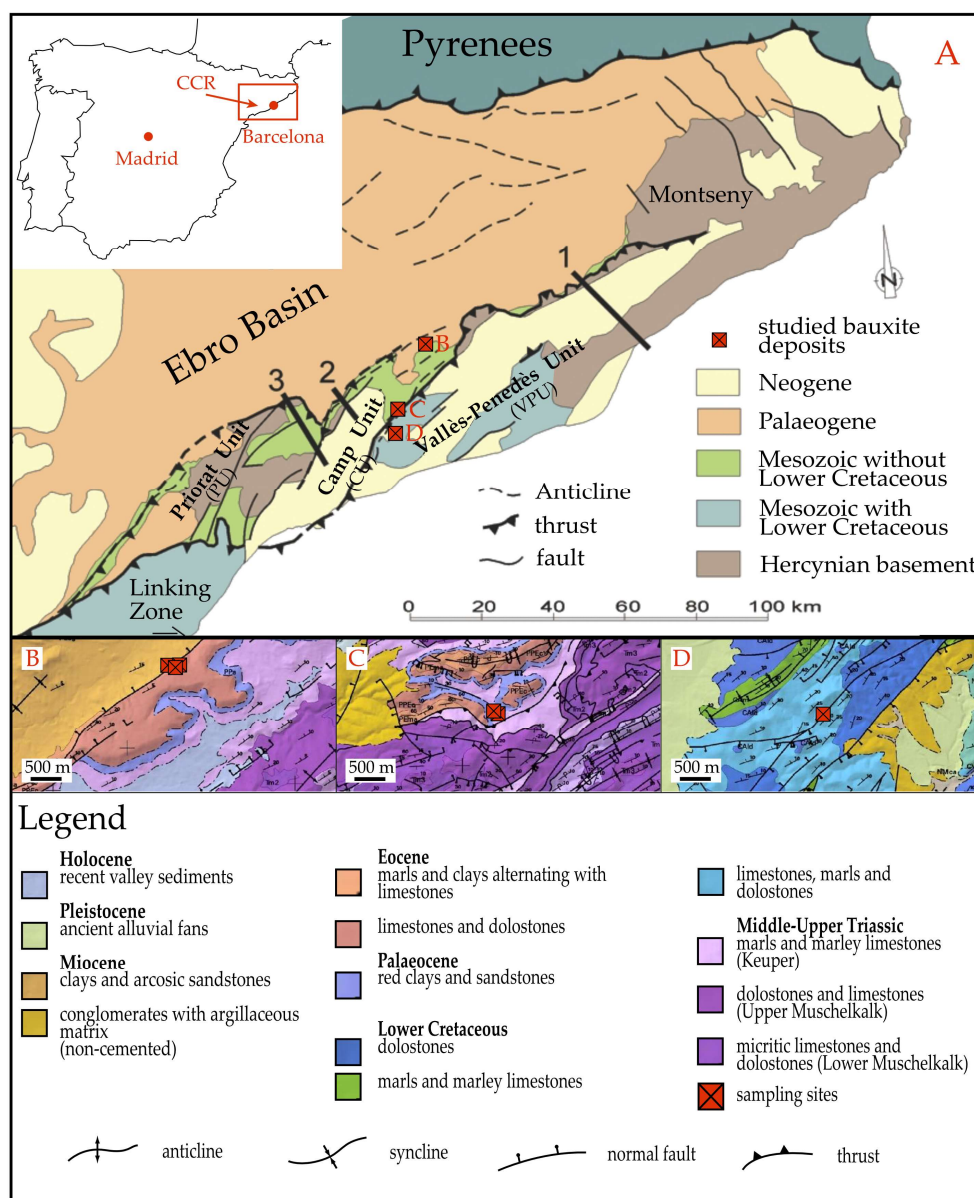


**Figure 1.** (A) Simplified geological map of the Catalan Coastal Range (CCR) modified from [42] and detailed geological maps of the studied bauxitic deposits in (B) the Plana de Casals area, (C) El Miracle mine and (D) the road-cutting near La Pineda de Santa Cristina modified from [43]. The location of the sampled outcrops is shown in (B–D). Note that the Barremian bauxite-filled analyzed karstic pockets are laterally limited in extent, occur on Triassic rocks and are overlain by Palaeocene and Eocene deposits. For an overview of the crustal structure of the CCR along cross-sections 1, 2 and 3 the reader is referred to [42].

The CCR represents the structural connection between the IC and the Pyrenees [44]. It is characterized by three thrust sheets: (1) Vallès-Penedès (VPU), (2) Camp (CU) and (3) Priorat (PU) which are situated on NE-verging thrusts. These thrusts, which are usually tens of kilometers in length, include the Hercynian basement and form a right-stepping, en-echelon array [41]. The strongest deformation is located in narrow bands along or near faults and associated monoclinical folds with strongly vergent or overturned limbs, whereas the internal parts of the thrust sheets are only slightly deformed [41].

The sedimentary record of the CCR comprises rocks of the Palaeozoic (Hercynian) basement which are restricted to outcrops on the NW margin of the CCR and Mesozoic to Cenozoic strata of the Alpine sedimentary cycle [45]. The onset of post-Hercynian sedimentation marks the initiation of the pre-orogenic stage during the Alpine sedimentary cycle. Deposition of fluvial red beds of Permian-Triassic age was followed by evaporite accumulations and carbonate deposition in an extensional tectonic setting that persisted until the Upper Jurassic. The associated complex tectono-sedimentary setting gave rise to a variety of marine sediments, such as carbonate-dolomitic breccia (related to an Early Liassic break-up platform due to rifting of the Atlantic Ocean), shallow marine platform carbonates, coastal deposits or basinal limestones and marls. The Late Jurassic-Early Cretaceous rifting cycle [46] resulted in a strong extensional regime with fragmentation, compartmentation and intense tilting of basement blocks, which led to prolonged periods of emergence of the NW sectors and the development of abundant lateritic horizons, as well as bauxite-filled karstic pockets in the Lower Barremian [47]. The main contractional stage during the Alpine orogeny started in the Late Eocene and continued until the Late Oligocene [42]. Deformation started in the NE and progressively moved to the SW, being related to the successive movement of the major NE-SW trending basement faults [45]. Many of the contractional structures in the CCR also contain a sinistral component, indicating that they most likely formed in a transpressive regime [45,48]. Paleogene sediments are mostly constrained to the southern margin of the Ebro basin [45]. The post-orogenic stage in the CCR is marked by Neogene extension related to the opening of the western Mediterranean Sea that started in the Lower Miocene and that persists until today [42,45]. The Neogene sedimentary record comprises a series of continental, lacustrine and lagoonal deposits with occasional marine transgressions which are limited to the Neogene troughs [45].

### 3. Sampling and Methodology

A total of eight samples from three different sampling sites in the CCR were collected (Figure 2), including four samples from an abandoned mine on the Plana de Casals (Figure 2A(i, ii)), three samples from the abandoned El Miracle mine near Les Pobles (Figure 2B(i, ii)) and one sample from a road cutting in La Pineda de Santa Cristina (LPSC) (Figure 2C(i, ii)) (Table 1).

Eleven thin sections (Table 1) covering the entire textural spectrum of every sampling site were produced. In addition, the samples were crushed and homogenized in order to obtain whole rock chemical and powder X-ray diffraction (XRD) analyses. Major, minor and trace elements (including REE) of the samples (approx. 10.5 g per sample) were determined at ActLabs Laboratories, Ontario, Canada, using fusion inductively coupled plasma emission spectroscopy (ICP-ES) and inductively coupled plasma mass spectrometry (ICP-MS).

The bulk mineralogical composition of the samples was studied by means of XRD in a PANalytical X'Pert Pro MPD Alpha1 powder diffractometer (PANalytical, Almelo, The Netherlands) in Bragg-Brentano  $\theta/2\theta$  geometry with a radius of 240 mm at the Centres Científics i Tecnològics, University of Barcelona (CCiT-UB), Spain. The ground samples were pressed into cylindrical standard sample holders (16 mm  $\times$  2.5 mm in size) using a glass plate to obtain a flat surface. Samples were scanned in increments of  $0.017^\circ$  from  $4^\circ$  to  $80^\circ$  using Cu  $K\alpha_1$  radiation ( $\lambda = 1.5406 \text{ \AA}$ ) at a voltage of 45 kV–40 mA and 150 s per scanning step. During the analysis, samples spun at two revolutions per second, while a variable automatic divergence slit maintained an illuminated length of 10 mm. The beam length was restricted to 12 mm in axial direction by a mask. An X'Celerator detector with an

active length of  $2.122^\circ$  was used. The software X'Pert HighScore<sup>®</sup> (Version 2.0.1, PANalytical, Almelo, The Netherlands) was used to subtract the background of the obtained patterns, to detect the peaks and to assign mineral phases to each peak, as well as to determine semi-quantitatively the mineral phases present in the powder samples. It has to be noted that results of semi-quantitative measurements may not be accurate for low concentrations (<5%) and therefore will be reported as traces.

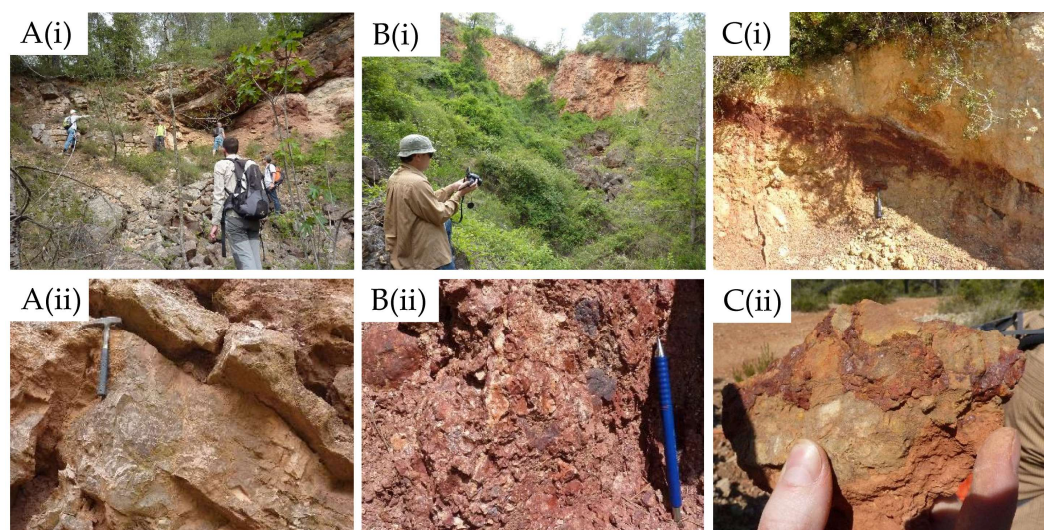


**Figure 2.** Field photographs of the sampled outcrops (i) and close-ups (ii) in the CCR: **A(i, ii)** Abandoned mine on the Plana de Casals, **B(i, ii)** abandoned mine El Miracle near Les Pobles, **C(i, ii)** road cutting close to La Pineda de Santa Cristina.

**Table 1.** Coordinates of the sampled sites in the CCR. All positions correspond to WGS84 UTM 31N.

Sample	Easting (m)	Northing (m)	Location	Thin Section
MM-1	378,151	4,595,059	Plana de Casals	MM-1
MM-2	378,342	4,595,064		MM-2
MM-3	378,342	4,595,064		MM-3
MM-4	378,291	4,595,024		MM-4 and MM4B
MI-0	369,239	4,579,639	Les Pobles (El Miracle Mine)	MI-0 and MI-0B
MI-1 (A, B)	369,239	4,579,639		MI-1A, MI-1Arep, MI-1B
MI-2	369,691	4,570,698		MI-2
RU-1	369,691	4,570,698	LPSC	-

One bauxitic sample (MM-4) was selected for the production of heavy mineral concentrates at the hydroseparation laboratory of the University of Barcelona [49]. To this end, the sample was dry- and wet-sieved using mesh sizes of 125  $\mu\text{m}$ , 75  $\mu\text{m}$  and 30  $\mu\text{m}$  and a target fraction of 30–75  $\mu\text{m}$  was selected. The 30–75  $\mu\text{m}$  fraction was further separated according to its magnetic properties by FRANTZ L-1 and LB-1 magnetic separators using working amperages of 0.4 A, 0.5 A, 0.8 A, 1.0 A and 1.65 A which resulted in six fractions. The six fractions (magnetic at 0.4, 0.5, 0.8, 1.0, 1.65 and non-magnetic at 1.65 A) were further treated using the computer-controlled hydroseparation (HS) device CNT HS-11 [50] applying the methodology for soft rock described in [51]. In contrast to these authors, HS was carried out after the magnetic separation. The densest grains separated by means of HS were embedded in cylindrical ( $d = 2.5 \text{ cm}$ ) resin mounts forming a thin “layer” (hereafter called monolayer) which was polished for further analysis.

The mineralogy and the textural features of the bauxitic samples were studied by means of transmitted and reflected light optical microscopy. The morphological and textural features, as well as the semi-quantitative composition of minerals in the selected samples (both monolayers and thin sections) were examined at CCiT-UB by means of scanning electron microscopy (SEM), using an environmental SEM Quanta 200 FEI, XTE 325/D8395 (Thermo Fisher Scientific, Waltham, MA, USA)

equipped with an energy dispersive spectrometer (EDS). The operating conditions were an accelerating voltage of 20 kV and a beam current of 1 nA. Additional electron micrographs and semi-quantitative analyses were obtained with a field emission scanning electron microscope (FE-SEM) Jeol JSM-7100 (JEOL, Ltd., Tokyo, Japan) at CCiT-UB. Quantitative chemical analyses were performed at the CCiT-UB using a JEOL JXA-8230 (JEOL, Ltd., Tokyo, Japan) electron probe micro analyzer (EPMA) operated in wavelength-dispersive spectroscopy (WDS) mode, with an accelerating voltage of 20 kV, 15 nA beam current and a varying beam diameter of ~1 to 5  $\mu\text{m}$  depending on grain size and mineralogy. The analytical standards and lines used for the analyses were: wollastonite (Si,  $K\alpha$ ), rutile (Ti,  $K\alpha$ ), corundum (Al,  $K\alpha$ ),  $\text{Fe}_2\text{O}_3$  (Fe,  $K\alpha$ ), rhodonite (Mn,  $K\alpha$ ), apatite (Ca,  $K\alpha$ ; P,  $K\alpha$ ; F,  $K\alpha$ ), barite (Ba,  $K\alpha$ ), celestine (Sr,  $K\alpha$ ),  $\text{UO}_2$  (U,  $M\beta$ ),  $\text{ThO}_2$  (Th,  $M\alpha$ ), GaAs (Ga,  $L\alpha$ ), metallic Co (Co,  $K\alpha$ ), YAG (Y,  $L\alpha$ ),  $\text{LaB}_6$  (La,  $L\alpha$ ),  $\text{CeO}_2$  (Ce,  $L\alpha$ ), REE-1 (Pr,  $L\beta$ ; Er,  $L\alpha$ ; Dy,  $L\beta$ ), REE-2 (Ho,  $L\beta$ ; Tm,  $L\alpha$ ; Eu,  $L\alpha$ ), REE-3 (Yb,  $L\alpha$ ; Sm,  $L\beta$ ),  $\text{Gd}_3\text{Ga}_5\text{O}_{12}$  (Gd,  $L\alpha$ ) and REE-4 (Lu,  $L\alpha$ ; Tb,  $L\alpha$ ; Nd,  $L\beta$ ). Micro-Raman spectra of the rare earth minerals and other minerals identified in the monolayers and thin sections were obtained with a HORIBA Jobin Yvon LabRam HR 800 dispersive spectrometer (Horiba, Ltd., Kyoto, Japan) equipped with an Olympus BXFM optical microscope (Olympus Corporation, Tokyo, Japan) at the CCiT-UB. Non-polarized Raman spectra were obtained in confocal geometry by applying a 532 and a 785 nm laser, using a  $100\times$  objective (beam size around 2  $\mu\text{m}$ ), with five measurement repetitions for 10 s each. In cases where the use of the 532 nm laser produced high fluorescence, the 785 nm laser was used. The instrument was calibrated by checking the position of the metallic Si band at  $\sim 520\text{ cm}^{-1}$ . The micro-Raman spectra were processed using the LabSpec<sup>®</sup> software (Version 5.33.14, Horiba, Ltd., Kyoto, Japan).

## 4. Results

### 4.1. Major and Trace Element Geochemistry and Geochemical Classification

Whole rock major, minor and trace element contents of the analyzed bauxitic samples are summarized in Table 2. Among the major element oxides,  $\text{Al}_2\text{O}_3$ ,  $\text{SiO}_2$ ,  $\text{Fe}_2\text{O}_3$  and  $\text{TiO}_2$  are those with the highest contents, which on the other hand show great variation. The average  $\text{SiO}_2$  content is 31 wt % but contents vary between 15 wt % (MM-1) and 38 wt % (MM-4).  $\text{Al}_2\text{O}_3$  behaves similarly, with contents varying between 27 wt % (MM-3) and 49 wt % (MM-1) (av. = 34.4 wt %). The  $\text{Fe}_2\text{O}_3$  contents also vary from 13 wt % to 29 wt % but are generally below 20 wt %. In contrast,  $\text{TiO}_2$  contents are rather constant in all samples ranging from 1.4 wt % to 2.3 wt %.  $\text{MgO}$ ,  $\text{Na}_2\text{O}$ ,  $\text{K}_2\text{O}$  and  $\text{CaO}$  contents are below 1 wt % for all samples except for sample RU-1 in which the  $\text{CaO}$  concentration is 2.5 wt %  $\text{CaO}$ .

Bauxitic samples yield contents higher than 100 ppm for elements such as V, Cr, Ni, Sr, and Zr, whereas the contents of other trace elements (Sc, Co, Ga, As, Nb, Mo, Ba, Pb, Hf, Th, U or Ga) are in the range of a few to tens of ppm (Table 2). The contents of Zn, Rb, Cs and Tl are generally close to or below their respective detection limits and are only relatively elevated in sample RU-1 (Table 2).

The  $\text{TiO}_2$  and  $\text{Al}_2\text{O}_3$  contents show a strong positive correlation (Figure 3B), suggesting that both Al and Ti behaved as relatively immobile elements during the bauxitization process. In contrast, the negative correlation observed between  $\text{SiO}_2$  and  $\text{Al}_2\text{O}_3$  (Figure 3A) points to retention of Al in the weathering profile as Si was leached. No correlation has been found for  $\text{Fe}_2\text{O}_3$  and  $\text{Al}_2\text{O}_3$  contents (Figure 3C) which indicates that Fe was mobile during the bauxitization process. Among the trace elements, the high field strength elements (HFSE, namely Nb, Ta, Zr, Th and U) show a correlation with  $\text{TiO}_2$  and  $\text{Al}_2\text{O}_3$ , with correlation coefficients close to or above 0.8 (Figure 3D–G). This indicates that these elements were rather immobile during the bauxitization process. In contrast, correlation between  $\text{TiO}_2$  and  $\text{Al}_2\text{O}_3$  with other elements, such as Ba, Pb, Sc, Y, V or Ni is poor or absent.

The studied bauxitic samples exhibit strongly varying REE contents with  $\Sigma\text{REE}$  in the range of 190 to 637 ppm, (av. = 372 ppm) (Table 2). LREE ( $\Sigma\text{LREE}$  = 156–541 ppm, av. = 329 ppm) are relatively enriched compared to HREE ( $\Sigma\text{HREE}$  = 23–96 ppm, av. = 44 ppm). The Y and Sc contents are in the

range of 35 to 148 ppm (av. = 64 ppm) and 29 to 64 ppm (av. = 45 ppm), respectively. Sc contents in the studied bauxitic samples are comparable to those of other Mediterranean karst bauxites (e.g., [21,52]). However, no correlation has been found for Sc and  $\text{Fe}_2\text{O}_3$  (Figure 3H), as has been described for karst bauxites of Parnassos-Ghiona [21]. The correlation between the contents of individual REE and  $\Sigma\text{REE}$  with those of  $\text{SiO}_2$ ,  $\text{Al}_2\text{O}_3$ ,  $\text{TiO}_2$  and MnO is poor, whereas the correlation between the contents of individual REE and  $\Sigma\text{REE}$  and the contents of  $\text{Fe}_2\text{O}_3$  and  $\text{P}_2\text{O}_5$  shows slightly negative and positive correlation, respectively (Figure 3I,J). The positive correlation between  $\text{P}_2\text{O}_5$  with  $\Sigma\text{REE}$  might indicate that phosphate phases are the main hosts of REE in the studied bauxitic ores. The samples yield heterogeneous LREE/HREE ratios between 4.6 and 10.6.

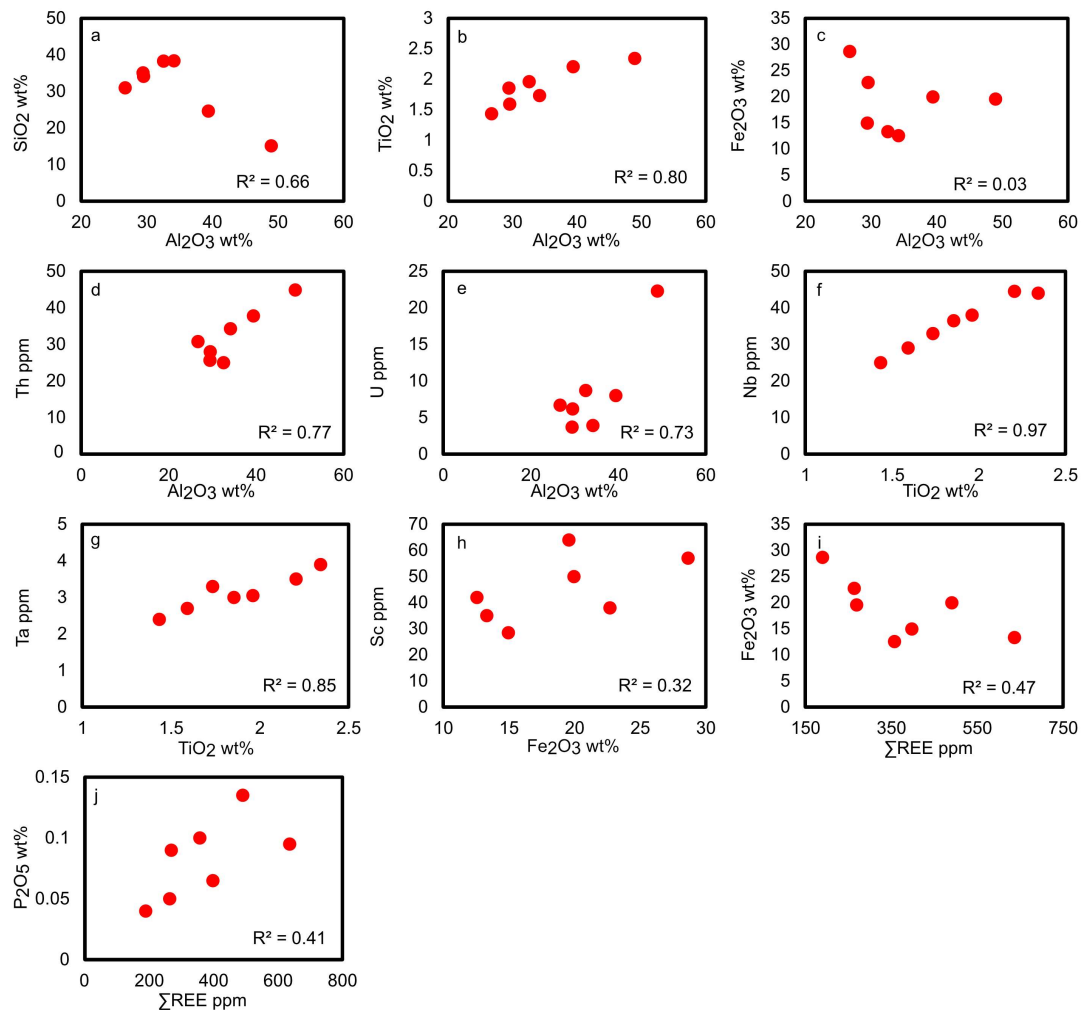


**Figure 3.** Selected Harker-type diagrams for major, minor and trace elements in the analyzed bauxitic samples. (A)  $\text{Al}_2\text{O}_3$  vs.  $\text{SiO}_2$ , (B)  $\text{Al}_2\text{O}_3$  vs.  $\text{TiO}_2$ , (C)  $\text{Al}_2\text{O}_3$  vs.  $\text{Fe}_2\text{O}_3$ , (D)  $\text{Al}_2\text{O}_3$  vs. Th, (E)  $\text{Al}_2\text{O}_3$  vs. U, (F)  $\text{TiO}_2$  vs. Nb, (G)  $\text{TiO}_2$  vs. Ta, (H)  $\text{Fe}_2\text{O}_3$  vs. Sc, (I)  $\Sigma\text{REE}$  vs.  $\text{Fe}_2\text{O}_3$ , (J)  $\Sigma\text{REE}$  vs.  $\text{P}_2\text{O}_5$ .

The  $\text{Ce}/\text{Ce}_N^*$  and  $\text{Eu}/\text{Eu}_N^*$  ratios were calculated from Equations (1) and (2) [53], and are reported in Table 2:

$$\text{Ce}/\text{Ce}_N^* = \text{Ce}_N / (0.5\text{La}_N + 0.5\text{Pr}_N) \quad (1)$$

where  $\text{Ce}_N^*$  is a background concentration, whereas  $\text{La}_N$  and  $\text{Pr}_N$  are chondrite-normalized La and Pr concentrations, respectively. The same equation structure was used for  $\text{Eu}/\text{Eu}_N^*$  (Equation (2)):

$$\text{Eu}/\text{Eu}_N^* = \text{Eu}_N / (0.5\text{Sm}_N + 0.5\text{Gd}_N) \quad (2)$$

Applying these equations reveals broadly constant, negative Eu-anomalies ( $\text{Eu}/\text{Eu}_N^* = 0.67\text{--}0.75$ ) and slightly negative, even though erratic Ce-anomalies ( $0.56\text{--}1.07$ ). The chondrite-normalized REE plot in Figure 4 reveals broadly similar distribution patterns for all samples, with negative slopes for LREE and fairly horizontal HREE segments. The overall negative slope geometry results from the relative enrichment of LREE to MREE ( $2.21 \leq \text{La}_N/\text{Sm}_N \leq 6.14$ ) and HREE ( $4.19 \leq \text{La}_N/\text{Yb}_N \leq 10.76$ ), and of MREE to HREE ( $1.89 \leq \text{Sm}_N/\text{Yb}_N \leq 2.50$ ).  $\text{Eu}/\text{Eu}_N^*$  consistently show negative anomalies ( $<0.8$ ), whereas Ce-anomalies are more erratic, but generally do not show anomalies (with the exception of a strong negative anomaly in sample MM-2). Furthermore, the overall enrichment in REE (and especially HREE) in sample MM-4 compared to the other bauxitic samples has to be highlighted (Table 2, Figure 4). The comparison of average chondrite-normalized REE contents of karst bauxite areas or deposits of the Mediterranean bauxite belt [20,21,34,40,52] with data from this study (Figure 4B) reveals broadly similar REE distribution patterns. They are characterized by negative slopes for LREE, relatively flat HREE patterns, pronounced negative Eu-anomalies and no Ce-anomalies. The major difference between displayed karst bauxites seems to be their overall REE content. Data for the Zagrad karst bauxite deposit, Montenegro [20] indicate much higher REE contents compared to the other karst bauxites. In contrast, REE contents in bauxites and bauxitic clays of Teruel, NE-Spain [40] are significantly lower. Interestingly, karst bauxites of the Parnassos-Ghiona deposits, Greece [21] show a positive Ce-anomaly which sets them apart from all other karst bauxites. The REE distribution pattern of the studied bauxitic samples is very similar to the average Italian bauxite REE distribution pattern (calculated from data for deposits in the Apulia, Campia and Abruzzi regions and Sardinia [52]).

**Table 2.** Major-, minor- and trace-element (including REE) concentrations of the studied bauxitic samples from the CCR.

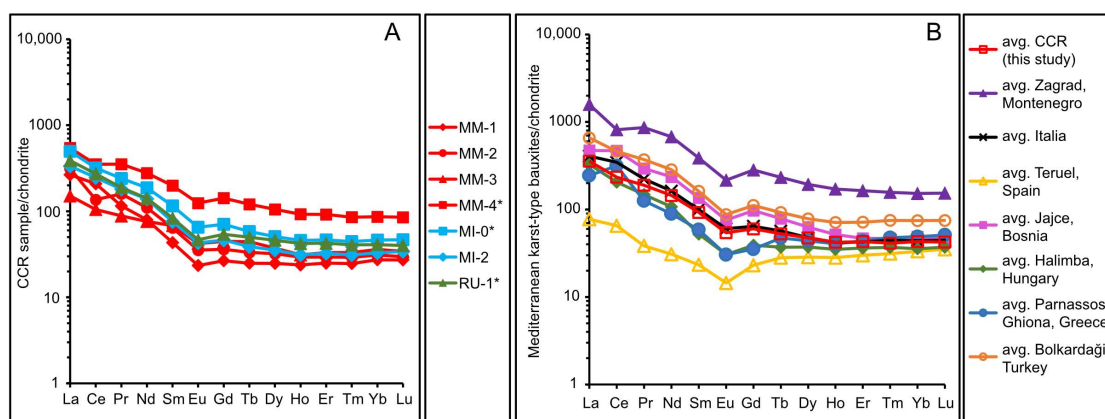
Sample Number	Plana de Casals				El Miracle Mine		LPSC
	MM-1	MM-2	MM-3	MM-4 <sup>1</sup>	MI-0 <sup>1</sup>	MI-2	RU-1 <sup>1</sup>
SiO <sub>2</sub> [wt %]	15.12	34.17	31.03	38.31	24.62	38.39	35.08
Al <sub>2</sub> O <sub>3</sub>	48.98	29.55	26.73	32.57	39.43	34.18	29.45
Fe <sub>2</sub> O <sub>3</sub> (T)	19.57	22.71	28.66	13.33	19.95	12.56	14.97
MnO	0.01	0.02	0.03	0.03	0.02	0.01	0.05
MgO	0.03	0.04	0.04	0.08	0.07	0.05	0.45
CaO	0.08	0.12	0.11	0.13	0.14	0.20	2.53
Na <sub>2</sub> O	0.02	0.02	0.02	0.03	0.03	0.04	0.06
K <sub>2</sub> O	0.02	0.03	0.02	0.14	0.13	0.06	0.49
TiO <sub>2</sub>	2.34	1.59	1.43	1.96	2.21	1.74	1.86
P <sub>2</sub> O <sub>5</sub>	0.09	0.05	0.04	0.10	0.14	0.10	0.07
LOI	12.77	11.55	10.67	12.78	12.36	12.96	14.77
Total	99.03	99.85	98.78	99.43	99.07	100.30	99.73
Ag [ppm]	1.50	1.10	0.90	1.50	2.00	1.30	1.40
As	29.00	32.00	45.00	28.00	38.50	18.00	13.00
Ba	32.00	19.00	12.00	41.50	39.00	23.00	78.50
Be	2.00	4.00	7.00	10.00	4.00	8.00	4.00
Bi	1.00	0.70	0.80	0.50	0.85	0.70	0.60
Co	6.00	6.00	15.00	16.00	21.50	18.00	13.00
Cr	400.00	230.00	270.00	155.00	280.00	220.00	145.00
Cs	<0.5	<0.5	<0.5	<0.5	<0.5	<0.5	8.35
Cu	20.00	20.00	30.00	20.00	30.00	50.00	40.00
Ga	63.00	30.00	39.00	32.00	52.00	39.00	33.00
Ge	2.00	2.00	2.00	2.00	2.00	1.00	2.00
Hf	12.60	8.20	8.10	10.80	14.00	11.80	9.90
In	0.30	0.20	0.20	< 0.2	0.25	0.20	< 0.2
Mo	19.00	5.00	6.00	7.00	17.00	8.00	3.00
Nb	44.00	29.00	25.00	38.00	44.50	33.00	36.50
Ni	70.00	70.00	90.00	90.00	125.00	130.00	135.00
Pb	29.00	43.00	41.00	58.50	55.00	41.00	35.50
Rb	<2	<2	<2	5.00	5.00	3.00	41.50
Sb	2.90	2.80	3.20	1.80	2.60	1.90	2.20
Sn	8.00	6.00	6.00	6.00	7.50	6.00	6.00



Table 2. Cont.

Sample Number	Plana de Casals				El Miracle Mine		LPSC
	MM-1	MM-2	MM-3	MM-4 <sup>1</sup>	MI-0 <sup>1</sup>	MI-2	RU-1 <sup>1</sup>
Sr	402.00	72.00	35.00	175.50	318.00	315.00	93.50
Ta	3.90	2.70	2.40	3.05	3.50	3.30	3.00
Th	44.90	28.00	30.80	25.00	37.80	34.30	25.70
Tl	0.10	0.10	0.30	0.10	<0.1	<0.1	1.25
U	22.30	6.20	6.70	8.70	8.00	3.90	3.70
V	531.00	360.00	471.00	244.50	393.50	303.00	238.00
W	4.00	3.00	3.00	4.00	4.50	3.00	5.50
Zn	<30	<30	<30	<30	65.00	40.00	170.00
Zr	508.00	332.00	317.00	434.50	556.00	466.00	397.00
Sc	64.00	38.00	57.00	35.00	50.00	42.00	28.50
Y	35.00	37.00	39.00	148.00	77.50	47.00	66.00
La	62.90	74.40	35.80	129.00	118.00	79.50	92.15
Ce	128.00	83.60	64.30	215.50	196.00	151.00	167.00
Pr	10.70	14.80	8.19	32.70	22.35	16.80	17.45
Nd	36.40	50.40	34.80	127.00	85.80	63.50	64.75
Sm	6.40	9.50	10.10	29.40	17.10	11.20	12.35
Eu	1.32	1.99	2.38	7.00	3.67	2.42	2.63
Gd	5.30	7.20	8.90	28.30	14.05	9.20	10.75
Tb	0.90	1.20	1.60	4.35	2.10	1.40	1.80
Dy	6.10	7.90	9.20	25.90	12.50	8.70	11.35
Ho	1.30	1.60	1.70	5.05	2.50	1.70	2.30
Er	4.00	4.70	5.30	14.70	7.45	5.20	6.80
Tm	0.61	0.72	0.82	2.11	1.10	0.77	1.01
Yb	4.40	5.00	5.80	13.90	7.45	5.30	6.60
Lu	0.67	0.73	0.84	2.10	1.15	0.84	0.99
$\Sigma$ REE <sup>2</sup>	269.00	263.74	189.73	637.01	491.22	357.53	397.92
$\Sigma$ LREE <sup>3</sup>	245.72	234.69	155.57	540.60	442.92	324.42	356.33
$\Sigma$ HREE <sup>4</sup>	23.28	29.05	34.16	96.41	48.30	33.11	41.59
$\Sigma$ REE+[Sc+Y]	368.00	338.74	285.73	820.01	618.72	446.53	492.42
LREE/HREE	10.55	8.08	4.55	5.61	9.17	9.80	8.57
La <sub>N</sub> /Yb <sub>N</sub> <sup>5</sup>	9.71	10.11	4.19	6.30	10.76	10.19	9.48
La <sub>N</sub> /Sm <sub>N</sub> <sup>6</sup>	6.14	4.89	2.21	2.74	4.31	4.43	4.66
Sm <sub>N</sub> /Yb <sub>N</sub> <sup>7</sup>	1.58	2.07	1.89	2.30	2.50	2.30	2.04
Ce/Ce <sub>N</sub> * <sup>8</sup>	1.07	0.56	0.85	0.76	0.84	0.93	0.92
Eu/Eu <sub>N</sub> * <sup>9</sup>	0.67	0.70	0.75	0.73	0.70	0.71	0.68

<sup>1</sup> MM-4, MI-0 and RU-1 = average of two measurements, <sup>2</sup>  $\Sigma$ REE =  $\Sigma$ (La-Lu), <sup>3</sup>  $\Sigma$ LREE =  $\Sigma$ (La-Eu), <sup>4</sup>  $\Sigma$ HREE =  $\Sigma$ (Gd-Lu), <sup>5</sup> La<sub>N</sub>/Yb<sub>N</sub> = (La/La<sub>N</sub>)/(Yb/Yb<sub>N</sub>), <sup>6</sup> La<sub>N</sub>/Sm<sub>N</sub> = (La/La<sub>N</sub>)/(Sm/Sm<sub>N</sub>), <sup>7</sup> Sm<sub>N</sub>/Yb<sub>N</sub> = (Sm/Sm<sub>N</sub>)/(Yb/Yb<sub>N</sub>), <sup>8</sup> Ce/Ce<sub>N</sub>\* and <sup>9</sup> Eu/Eu<sub>N</sub>\* after [53], Fe<sub>2</sub>O<sub>3</sub>(T) = total iron, LOI = loss on ignition.



**Figure 4.** (A) Chondrite-normalized REE plot for whole rock data of the studied bauxitic samples of the CCR, MM-4\*, MI-0\*, RU-1\* = average of two measurements. (B) Chondrite-normalized average REE contents of several karst-type bauxite areas or deposits within the Mediterranean bauxite belt (this study and literature for comparison [20,21,34,40,52]). Normalization values are from [54].

In the  $\text{SiO}_2\text{-Fe}_2\text{O}_3\text{-Al}_2\text{O}_3\text{+TiO}_2$  classification diagram after [22], in Figure 5, most of the studied bauxitic samples plot in the clayey or iron-rich bauxite fields, whereas the samples with the highest  $\text{Fe}_2\text{O}_3$  contents (MM-2, MM-3) fall in the bauxitic iron ore field.

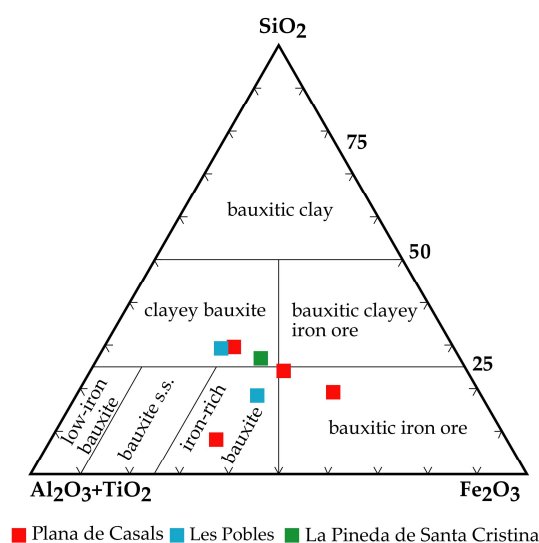


**Figure 5.** Whole rock  $\text{SiO}_2\text{-Fe}_2\text{O}_3\text{-Al}_2\text{O}_3\text{+TiO}_2$  ternary plot of the studied bauxitic samples; bauxite classification fields are after [22].

## 4.2. Mineralogy

### 4.2.1. Mineralogical and Textural Characteristics and Classification of CCR Bauxites

Powder-XRD analysis revealed that the studied bauxitic samples are mainly composed of phyllosilicates, Fe-oxides, Al-oxyhydroxides, Ti-oxides, as well as calcite in certain quantities (Table 3). The most abundant mineral is kaolinite (38–96 wt %). Hematite is the only mineral of the Fe-oxide and Fe-hydroxide-groups detected and is present in all samples (traces to 27 wt %), as are the Ti-oxides anatase (traces) and rutile (traces to 5 wt %). Moreover, two samples (namely MM-1 and MI-0) contain significant amounts of boehmite [ $\gamma\text{-AlO}(\text{OH})$ ] (23–33 wt %) and diasporite [ $\alpha\text{-AlO}(\text{OH})$ ] (6–8 wt %). It is worth noting the absence of gibbsite in all the analyzed samples. In samples MI-1B, MI-2 and RU-1, calcite has been detected (traces to 26 wt %). Furthermore, sample RU-1 also contains 32 wt % of nacrite.

**Table 3.** Semi-quantitative mineral composition obtained by XRD-analysis (wt %) of the studied bauxitic samples from the CCR.

Sample No.	Kln	Nac	Hem	Bhm	Dsp	Rt	Ant	Cal
MM-1	38	-	16	33	6	tr	tr	-
MM-2	73	-	19	-	-	tr	tr	-
MM-3	74	-	18	-	-	5	tr	-
MM-4	76	-	16	-	-	tr	tr	-
MI-0	45	-	17	23	8	tr	tr	-
MI-1A <sup>1</sup>	96	-	tr	-	-	-	-	-
MI-1B <sup>2</sup>	45	-	27	-	-	-	tr	26
MI-2	75	-	14	-	-	5	tr	tr
RU-1	37	32	13	-	-	tr	tr	10

<sup>1</sup> MI-1A = red, soft sample fragment, <sup>2</sup> MI-1B = dark red, oxide-rich sample fragment; Kln = kaolinite, Nac = nacrite, Hem = hematite, Bhm = boehmite, Dsp = diasporite, Rt = rutile, Ant = anatase, Cal = calcite, tr = traces. Mineral abbreviations from [55].

In the clay mineral-Fe mineral-Al + Ti mineral classification diagram from [22] in Figure 6, the studied bauxitic samples plot in the bauxitic clay and clayey bauxite fields. Samples are thus characterized by relatively low aluminium and high silica contents, respectively. Several of the analyzed samples actually are no bauxites *sensu stricto* (even though the geochemical classification after [22] in Figure 5 suggests this), but correspond to bauxitic clays. Therefore, the most appropriate term to describe the studied samples would be “bauxitic ore”. It is important to highlight that the classification scheme of [22] (which is broadly used in literature) in its original sense was actually conceived for semi-quantitative XRD data. From the comparison of Figures 5 and 6 it is evident that the use of whole rock geochemical data for bauxite classification might be misleading at times, since Figure 5 indicates that studied bauxitic ores mainly correspond to iron-rich bauxite or bauxitic iron ore and clayey bauxite even though the majority of the studied samples are lacking in Al-oxyhydroxides (Table 3).

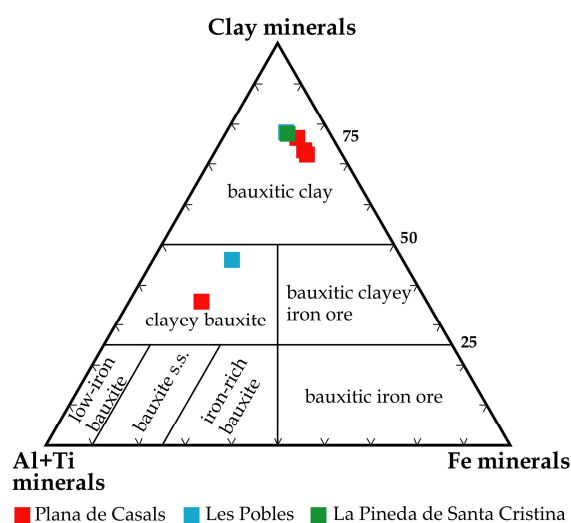


**Figure 6.** Ternary clay mineral-Fe mineral-Al+Ti mineral plot of the studied bauxitic samples based on results of semi-quantitative X-ray diffraction; bauxite classification fields after [22].

Bauxitic ores from the CCR exhibit a great variety of textures which are illustrated in Figure 7; such textural features are shared by all the studied deposits. Most of the studied samples show a breccia texture characterized by bauxite clasts and pebbles that vary considerably in size (up to 100 mm) and that are embedded in a pelitomorph matrix dominated by kaolinite and small-sized clastic particles (Figure 7A). Fractures and cavities are typically filled with kaolinite and locally calcite. Samples with a breccia texture show abundant mm-sized bauxite clasts/ roundgrains with a pelitomorph matrix containing micro-ooids (Figure 7B), even though some are homogenous inside in which case they are typically made up almost exclusively of kaolinite (Figure 7C). The brownish-red color of the matrix surrounding the bauxite clasts and pebbles indicates iron impregnations (Figure 7C). Locally, ooido-pisoidic textures have also been observed (Figure 7D) (*sensu* [22]). Fe-rich ooids and pisoids are dominantly dark red to reddish brown in color and appear opaque in transmitted light (Figure 7E). These ooids and pisoids show equivalent concentric structures as Al-rich ooids (Figure 7F). The image in Figure 7G illustrates a texturally complex mm-sized pisoid made up of fine-grained clastic fragments of Fe-oxides, surrounded by a layer of ooidic texture with Fe-rich ooids within a matrix of Al-oxyhydroxides; towards the boundaries of the pisoid concentric alternating layers of Al- and Fe-oxyhydroxides occur. In one sample, fractures across the matrix are filled with a highly reflective material (Figure 7H) and its texture resembles features typical of plant cells. This potential plant debris is strongly fragmented and might be attributed to macerals (probably fusinite and inertodetrinite of the inertinite group). However, SEM-EDS and micro-Raman analysis proved that this material is composed of hematite instead of organic-rich compounds.

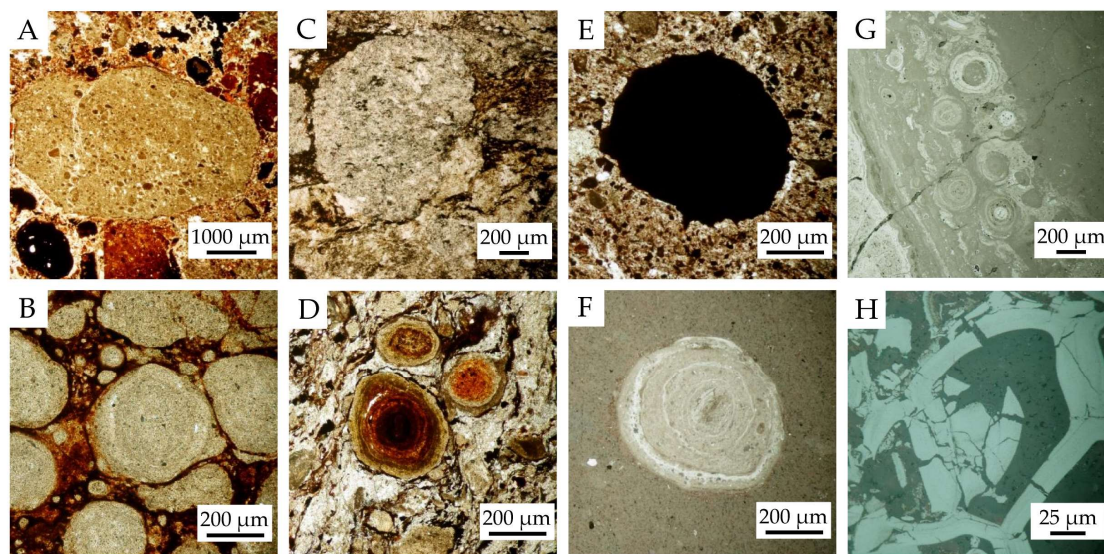


**Figure 7.** Transmitted, plane polarized (A–E) and reflected (F–H) light microphotographs of components and textures of the bauxite deposits from the CCR. (A) Bauxite roundgrains with local micro-oids (<100  $\mu\text{m}$ ). (B) Detail of bauxite roundgrains. (C) Close-up of a bauxite clast made up of kaolinite and surrounded by a brown, aphanitic matrix. (D) Ooidic texture in which the whitish matrix is made up of kaolinite and the ooids are made up of Fe- and Al-oxyhydroxides. (E,F) Close-up of a Fe-rich ooid in transmitted (E) and reflected (F) light. (G) Complex concentric outer rim of a mm-sized pisoid. Note the similarity to Fe-rich ooids. (H) Reflected light view of detritus that resemble textures developed by plant cells corresponding to hematite mineralization.

#### 4.2.2. REE Mineralogy

Thirty-six REE-bearing mineral grains were found in heavy mineral concentrates (4 grains) and in thin sections (32 grains). The REE mineralogy in the bauxitic ores is dominated by two types of phosphate minerals: monazite-(Ce) and xenotime-(Y). Two grains recovered from heavy mineral concentrates are >50  $\mu\text{m}$  in size (Figure 8A,B). Grain sizes in thin sections are typically <10  $\mu\text{m}$  with the largest grains being ~20  $\mu\text{m}$  across. Most REE-phosphates occur embedded in the aphanitic matrix composed of kaolin minerals (Figure 8C,D,F,G). However, some grains are observed in contact with Fe-oxides (Figure 8E) or Fe-impregnated parts of the kaolin mineral-rich matrix. REE phosphate grains show evidence for both detrital and authigenic origin. Whereas euhedral to subhedral crystals (Figure 8B), rounded grain edges and oval to elongated grain shapes (Figure 8D) point to a detrital origin, concentric growth textures (Figure 8F), intergrowth of grains with the kaolin mineral-rich matrix (Figure 8F) or irregular grain morphologies are indicative of an authigenic origin. A slightly brighter aureole around a xenotime grain of triangular shape is interpreted as an alteration rim of a detrital grain (Figure 8G). Figure 8C illustrates a common textural relationship between rare earth minerals, the matrix and other components of the bauxitic samples *in-situ*. Here, a monazite-(Ce) grain embedded in the kaolin mineral-rich matrix is associated with anatase and zircon grains.

Representative Raman spectra of REE-phosphates using a 532 nm wavelength laser are given in Figure 9. The comparison of a Raman spectrum obtained in a monazite-(Ce) grain with a reference spectrum [56] of this mineral reveals a good correlation between bands at ~969 and ~1057  $\text{cm}^{-1}$ . The comparison of a Raman spectrum obtained in a xenotime-(Y) grain with a reference spectrum [56] of this mineral yields a good correlation between bands at ~997, ~1022 and ~1053  $\text{cm}^{-1}$ , as well as in the range from 300 to 700  $\text{cm}^{-1}$ . The Raman bands at ~1000  $\text{cm}^{-1}$  correspond to the characteristic  $\text{PO}_4$ -stretching vibrations [57].

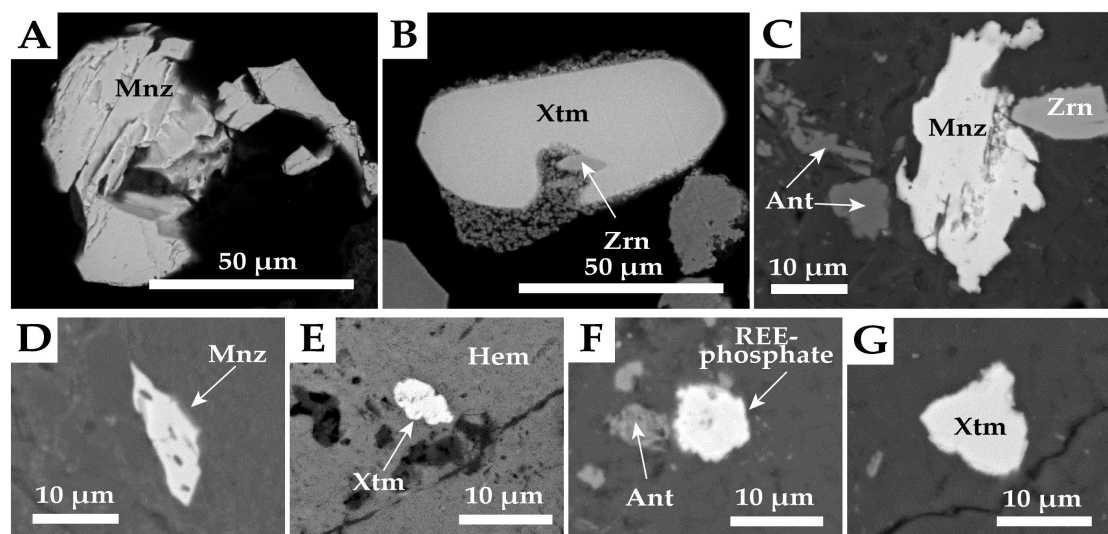


**Figure 8.** Backscattered-electron (BSE) images of REE-phosphates found in bauxitic ores from the CCR. (A,B) Monazite-(Ce) and xenotime-(Y) grains recovered from heavy mineral concentrates. The monazite-(Ce) crystal shows a sharp, irregular outline and abundant scratches. The xenotime-(Y) crystal is subhedral and shows slightly rounded and locally embayed outlines and pyramidal termination; it contains a small-sized zircon grain. (C–G) Monazite-(Ce) and xenotime-(Y) grains discovered in thin sections. (C) Textural relationships between an anhedronal monazite-(Ce) grain floating in the kaolin mineral-rich matrix along with a zircon and several anatase grains. (D) Minute anhedronal monazite-(Ce) grain embedded in the kaolin mineral-rich matrix. (E) Minute xenotime-(Y) grain hosted by porous hematite. (F) REE-phosphate with a concentric texture and intergrowth with the kaolin mineral-rich matrix. (G) Anhedronal xenotime grain with an alteration rim. Mnz = monazite-(Ce), Xtm = xenotime-(Y), Zrn = zircon, Ant = anatase, Hem = hematite.

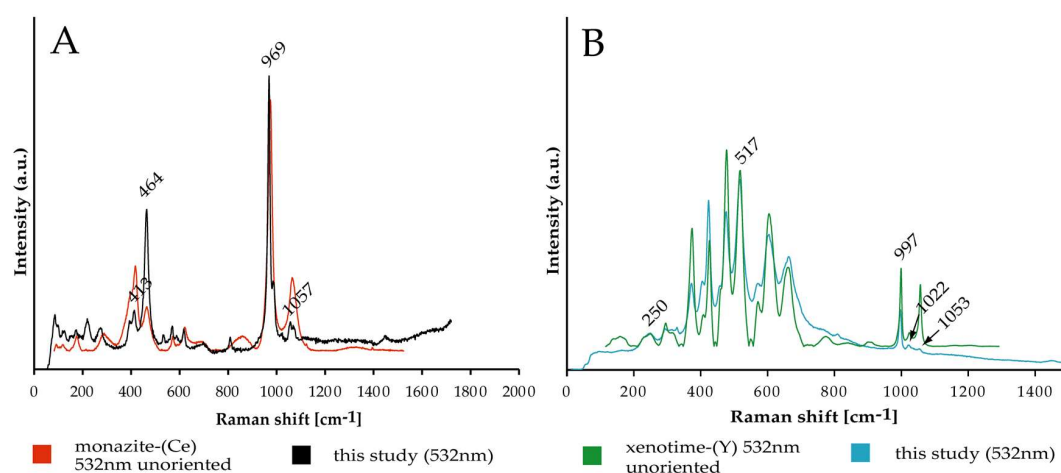


**Figure 9.** Representative Raman spectra of monazite-(Ce) and xenotime-(Y) grains recovered from heavy mineral concentrates of bauxitic ores of the CCR. (A) Monazite spectrum obtained with a 532 nm wavelength laser. (B) Xenotime-(Y) spectrum obtained with a 532 nm wavelength laser. Reference spectra for comparison in (A) and (B) were taken from [56]. a.u. = arbitrary units.

The studied monazite-(Ce) and xenotime-(Y) grains have relatively low ThO<sub>2</sub> (av. =1.07 wt %; 0.014 atoms per formula unit, a.p.f.u., Th, normalized to 4 oxygens), UO<sub>2</sub> (av. =0.33 wt %, 0.003 a.p.f.u.) and CaO (av. =0.26 wt %) (Table 4) contents. Monazite-(Ce) shows systematically higher ThO<sub>2</sub> than xenotime-(Y) in which ThO<sub>2</sub> contents commonly lie below the detection limit (d.l.) for EPMA. MnO, BaO and SrO generally are below detection limit. SiO<sub>2</sub>, Al<sub>2</sub>O<sub>3</sub>, TiO<sub>2</sub> and FeO contents are mostly below 1 wt % and may, at least partially, be attributed to measurement errors due to the small grain

sizes of the rare earth minerals. Ce (av. =0.43 a.p.f.u.) is the dominant REE in monazite grains along with less abundant La (av. = 0.2 a.p.f.u.), Nd (av. = 0.19 a.p.f.u.), Gd (av. = 0.04 a.p.f.u.) and Sm (av. = 0.03 a.p.f.u.). The dominant REE in xenotime-(Y) is Y (av. = 0.69 a.p.f.u.) along with minor Dy (av. = 0.06 a.p.f.u.), Er, Yb (both av. = 0.04 a.p.f.u.) and Gd (av. = 0.03 a.p.f.u.). Most EPMA analyses showed analytical totals ~100%, and approach near ideal stoichiometry (total A site cations equal ~0.93 and ~0.96 a.p.f.u. in monazite and xenotime, respectively and total B site cations equal ~1.16 and ~1.14 a.p.f.u. in monazite and xenotime, respectively).

**Table 4.** Representative EPMA analyses of monazite-(Ce) (left) and xenotime-(Y) (right) grains in heavy mineral concentrates and thin sections of the bauxitic samples of the CCR.

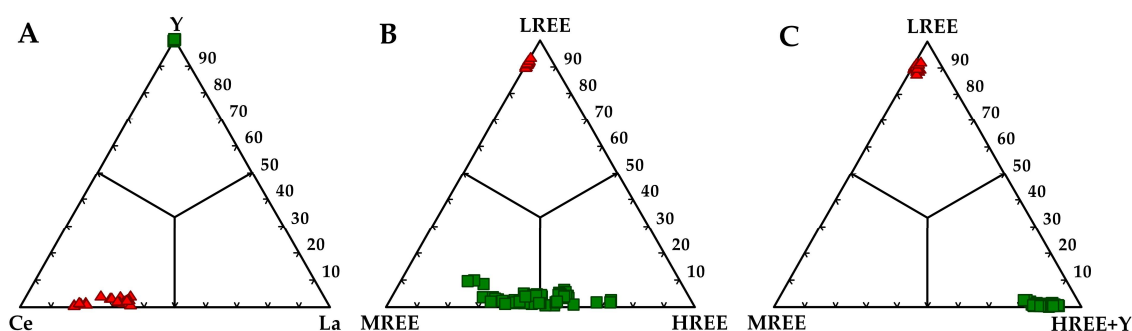
No.	MM-4 p1	MM-4 p6	0.4 A mag. FC* p10	0.4 A mag. FC* p13	MM-4 p13	MM-2 p22	0.4 A mag. FC p1	0.4 A mag. FC p6
P <sub>2</sub> O <sub>5</sub> (wt %)	28.19	28.42	28.44	27.12	35.41	34.41	34.94	35.12
SiO <sub>2</sub>	d.l.	1.64	0.04	d.l.	d.l.	1.25	0.04	d.l.
TiO <sub>2</sub>	0.20	0.25	d.l.	d.l.	0.02	0.39	0.04	d.l.
Al <sub>2</sub> O <sub>3</sub>	0.48	2.73	d.l.	0.01	0.16	0.36	d.l.	d.l.
FeO	0.14	0.17	0.30	0.20	0.61	0.84	0.84	0.87
MnO	d.l.	d.l.	d.l.	d.l.	0.00	0.00	0.00	d.l.
CoO	0.03	0.02	0.02	0.01	0.45	0.28	0.40	0.38
BaO	d.l.	d.l.	d.l.	d.l.	d.l.	0.00	0.04	0.02
SrO	0.02	d.l.	0.03	0.03	d.l.	0.11	d.l.	d.l.
CaO	1.16	0.24	0.25	0.27	0.07	0.19	0.12	0.08
Ga <sub>2</sub> O <sub>3</sub>	0.31	0.06	0.18	0.24	0.24	0.04	0.25	0.11
Y <sub>2</sub> O <sub>3</sub>	1.03	0.36	0.42	0.41	41.83	41.03	39.02	39.77
ThO <sub>2</sub>	4.55	0.80	1.89	1.82	d.l.	1.00	0.03	0.00
UO <sub>2</sub>	0.19	0.05	0.26	0.18	0.29	0.02	0.43	0.69
La <sub>2</sub> O <sub>3</sub>	12.70	6.76	15.79	16.74	0.04	0.00	0.09	0.11
Ce <sub>2</sub> O <sub>3</sub>	27.55	29.49	31.76	31.29	0.12	0.00	0.07	0.13
Pr <sub>2</sub> O <sub>3</sub>	2.96	3.89	2.83	3.11	0.05	0.02	0.02	d.l.
Nd <sub>2</sub> O <sub>3</sub>	13.17	18.74	12.40	12.56	0.63	0.15	0.80	0.64
Sm <sub>2</sub> O <sub>3</sub>	1.76	1.96	2.02	2.09	0.56	0.54	1.06	0.94
Eu <sub>2</sub> O <sub>3</sub>	0.99	1.25	0.98	0.96	0.12	0.37	d.l.	0.05
Gd <sub>2</sub> O <sub>3</sub>	2.86	2.46	3.27	3.15	2.09	3.51	3.26	2.98
Tb <sub>2</sub> O <sub>3</sub>	d.l.	d.l.	d.l.	d.l.	0.44	0.78	0.93	0.74
Dy <sub>2</sub> O <sub>3</sub>	0.43	0.32	0.27	0.44	4.95	5.98	6.57	6.33
Ho <sub>2</sub> O <sub>3</sub>	0.04	d.l.	d.l.	d.l.	1.11	1.09	0.90	0.91
Er <sub>2</sub> O <sub>3</sub>	0.02	d.l.	d.l.	d.l.	4.42	3.38	3.87	4.06
Tm <sub>2</sub> O <sub>3</sub>	0.26	0.18	0.16	0.24	0.73	0.34	0.66	0.72
Yb <sub>2</sub> O <sub>3</sub>	d.l.	d.l.	d.l.	d.l.	4.41	2.17	3.89	4.27
Lu <sub>2</sub> O <sub>3</sub>	0.02	d.l.	d.l.	0.00	0.78	0.44	0.69	0.73
F	1.01	0.87	0.91	1.05	1.85	1.82	1.86	1.89
SUM	100.07	100.66	102.22	101.92	101.38	100.51	100.82	101.54
P (a.p.f.u.) <sup>1</sup>	0.93	0.89	0.94	0.91	0.96	0.93	0.96	0.96
Si	-	0.06	0.00	-	-	0.04	0.00	-
SUM A	0.93	0.95	0.94	0.91	0.96	0.97	0.96	0.96
Ti	0.01	0.01	-	-	0.00	0.01	0.00	-
Al	0.02	0.12	-	0.00	0.01	0.01	-	-
Fe	0.01	0.01	0.01	0.01	0.02	0.02	0.02	0.02
Mn	-	-	-	-	0.00	-	0.00	-
Co	0.00	0.00	0.00	0.00	0.01	0.01	0.01	0.01
Ba	-	-	-	-	-	-	0.00	0.00
Sr	0.00	-	0.00	0.00	-	0.00	-	-
Ca	0.05	0.01	0.01	0.01	0.00	0.01	0.00	0.00
Ga	0.01	0.00	0.01	0.01	0.01	0.00	0.01	0.00
Th	0.04	0.01	0.02	0.02	-	0.01	0.00	0.00
U	0.00	0.00	0.00	0.00	0.00	0.00	0.00	0.01
Y	0.02	0.01	0.01	0.01	0.71	0.69	0.67	0.68
La	0.18	0.09	0.23	0.24	0.00	0.00	0.00	0.00
Ce	0.39	0.40	0.45	0.45	0.00	-	0.00	0.00
Pr	0.04	0.05	0.04	0.05	0.00	0.00	0.00	-
Nd	0.18	0.25	0.17	0.18	0.01	0.00	0.01	0.01
Sm	0.02	0.03	0.03	0.03	0.01	0.01	0.01	0.01
Eu	0.01	0.02	0.01	0.01	0.00	0.00	-	0.00

Table 4. Cont.

No.	MM-4 p1	MM-4 p6	0.4 A mag. FC* p10	0.4 A mag. FC* p13	MM-4 p13	MM-2 p22	0.4 A mag. FC p1	0.4 A mag. FC p6
Gd	0.04	0.03	0.04	0.04	0.02	0.04	0.04	0.03
Tb	-	-	-	-	0.01	0.01	0.01	0.01
Dy	0.01	0.00	0.00	0.01	0.05	0.06	0.07	0.07
Ho	0.00	-	-	-	0.01	0.01	0.01	0.01
Er	0.00	-	-	-	0.04	0.03	0.04	0.04
Tm	0.00	0.00	0.00	0.00	0.01	0.00	0.01	0.01
Yb	-	-	-	-	0.04	0.02	0.04	0.04
Lu	0.00	-	-	0.00	0.01	0.00	0.01	0.01
F	0.12	0.10	0.11	0.13	0.19	0.18	0.19	0.19
SUM B	1.16	1.13	1.14	1.20	1.15	1.14	1.15	1.15

d.l. = below detection limit, <sup>1</sup> a.p.f.u. = atoms per formula unit, cations normalized to 4 oxygens.

Ternary Y-La-Ce, LREE-HREE-MREE and LREE-HREE+Y-MREE plots in Figure 10 reveal the distribution of LREE, MREE and HREE in the analyzed monazite-(Ce) and xenotime-(Y) grains. They show that monazite-(Ce) is enriched in LREE, whereas xenotime-(Y) is enriched in MREE and HREE.



**Figure 10.** Ternary (A) Y-La-Ce, (B) LREE-HREE-MREE, (C) LREE-HREE+Y-MREE plots of the REE compositions of analyzed monazite (red triangles) and xenotime (green squares) grains in bauxitic samples of the CCR. Note that the REE composition in xenotime is considerably more varied than in monazite (B). LREE =  $\sum$ La-Pm, MREE =  $\sum$ Sm-Dy, HREE =  $\sum$ Ho-Lu.

#### 4.2.3. Other Mineral Phases in Heavy Mineral Concentrates

Apart from REE-phases, heavy mineral concentrates also contain hematite, sulfides (pyrite and an unidentified NiFe-sulfide), Ti-oxides (rutile, anatase), baddeleyite and zircon. Hematite and sulfides are dominant in concentrates separated at 0.4 and 0.5 A. In contrast, zircon and Ti-oxides are more abundant in non-magnetic concentrates at higher amperages along with a few baddeleyite grains. Sulfide grains are usually anhedral crystals that often show triangular breakout on the polished surfaces and rounded edges. Hematite and Ti-oxide grains are mostly of irregular shape with smooth or flaky appearance and variable porosity. In contrast, zircon typically occurs as euhedral to subhedral, elongated to equidimensional prismatic crystals that locally show pyramidal terminations and are usually larger than 50  $\mu$ m across. Zircon crystals exhibit aspect ratios between 1 and 3.4 (av. = 1.7). Some zircon crystals occur as inclusions within xenotime-(Y) (Figure 8B). Baddeleyite crystals are largely <20  $\mu$ m across. These crystals have sharp edges and a rectangular appearance.

## 5. Discussion

### 5.1. Bauxite Ore Formation

Unlike lateritic bauxites, which are usually directly related to their underlying precursor rocks [23], the parental material of karst bauxites often remains ambiguous [22,30]. Many different types of source rocks have been proposed, including argillite components of the underlying limestone [58],

volcanic ash [59], basement rock debris [22], lateritic clays [39], wind-borne material [60], slates [34] or argillaceous material [26].

Although it is proven that fractionation of major, minor and trace elements does occur during bauxitization [26,29,58,61], it is widely accepted that the study of immobile elements is a powerful tool to unravel the parental material and the genetic history of karst bauxites [30]. Therefore, the identification of mobile and immobile elements during the bauxitization process is of vital importance. In this study, the observed positive correlation between  $\text{TiO}_2$  and  $\text{Al}_2\text{O}_3$  (Figure 3B) might be attributed to the fact that Al-oxyhydroxides have been found to contain Ti-nanominerals, as was demonstrated for karst bauxite deposits of Parnassos-Ghiona, Greece [62]. Trace elements, such as Nb, Ta, Zr, Th or U show a good correlation with  $\text{TiO}_2$  and  $\text{Al}_2\text{O}_3$ , meaning that they also behaved rather immobile during bauxitization. In the case of Th and U, the correlation with  $\text{Al}_2\text{O}_3$  might be attributed to adsorption of these elements to clay minerals. Hence, both Th and U are thought to be mainly hosted in the kaolin mineral-rich matrix and not in Al-oxyhydroxide phases. Furthermore, it has been shown that Ti-oxides in bauxite can accumulate substantial amounts of Nb, Ta, Th and U [63]. The good correlation between Nb and Ta with TiO might indicate that in the studied bauxitic samples these elements are hosted in Ti-oxide phases (Figure 3F,G). In literature, the  $\text{Al}_2\text{O}_3/\text{TiO}_2$  ratio has been used to identify bauxite protoliths (e.g., [30,40,64]). However, it needs to be stressed that this ratio only reflects the protolith values if both Al and Ti behave conservatively. This is the case, among others, in bauxite ores from the Nurra district in Sardinia [30] and in bauxites from Teruel, Linking Zone, NE-Spain [38,40]. Eu-anomalies also represent an index of chemical differentiation that is retained even during intense weathering [65]. As such, it may also be used to identify the precursor material of bauxites. Recently, Sm/Nd plotted vs.  $\text{Eu}/\text{Eu}_{\text{N}}^*$  has also been successfully applied to identify parental material of bauxite rocks [32]. Özlü [66] used Zr/Cr/Ga ratios to constrain the precursor material of karst bauxites, where Zr represents a characteristic element for acidic rocks, whereas Ga and Cr are representative for intermediate and ultrabasic rocks, respectively.

The correlation between  $\text{Al}_2\text{O}_3$  and  $\text{TiO}_2$  contents in the studied samples yields a correlation coefficient ( $R^2$ ) of  $\sim 0.8$  (Figure 3B). Since  $R^2$  is  $>0.8$  [67], we assume that the proportions between these two elements were mostly unaffected during the bauxitization process and hence, that the analyzed  $\text{TiO}_2/\text{Al}_2\text{O}_3$  ratio is representative of the parent rock. The  $\text{Eu}/\text{Eu}_{\text{N}}^*-\text{TiO}_2/\text{Al}_2\text{O}_3$  systematics of CCR bauxites plot close to the average composition of the upper continental crust (UCC) and lie halfway between  $\text{Eu}/\text{Eu}_{\text{N}}^*-\text{TiO}_2/\text{Al}_2\text{O}_3$  compositions of felsic volcanic and basaltic rocks (Figure 11A). A similar trend is observed using the Sm/Nd vs.  $\text{Eu}/\text{Eu}_{\text{N}}^*$  plot (Figure 11B) after [32]. In the Zr-Cr-Ga ternary plot after [66] bauxite compositions also plot close to the composition of the UCC and lie in the field of intermediate magmatic or argillaceous (with Zr-Cr between basic and acidic compositions) parent rocks. Some analyses approximate the field of acidic precursor materials (Figure 11C). Geochemical data suggest that the precursor material of the studied bauxitic ores was of argillaceous sedimentary composition, possibly derived from intermediate igneous rocks.

This constraint is indeed in good agreement with the occurrence of accessory detrital minerals, such as zircon, baddeleyite, monazite-(Ce) and xenotime-(Y) (i.e., mineral species highly resistant to weathering that are more common in intermediate to acidic rocks). Their presence points to a possible contribution of weathered aluminosilicate rocks of igneous origin to the precursor material. Whether this contribution is of direct or indirect nature (i.e., eroded from lateritized igneous rocks vs. eroded from lateritized sedimentary rocks) is difficult to determine with the available data.

Abundant hematite further constrains bauxite formation conditions since it is generally associated with a vadose, highly oxidizing environment [68], with hematite formation at a maximum at neutral to slightly alkaline conditions (pH 7–8). Moreover, its presence implies epigenetic processes during bauxitization, including Fe-mobilization, Fe-precipitation as amorphous Fe-hydroxides and subsequent recrystallization to hematite during diagenesis. In this context hematite was shown to form contemporaneously to Al-oxyhydroxides [62].



Bauxite deposits of the CCR rest on Lower Jurassic [47] or Middle Triassic [36] footwall carbonates and are covered by Paleogene (Paleocene or Eocene) siliciclastic deposits of the Ebro basin. Despite the large depositional gap of >120 Ma, Combes [47] suggests a Late/Post-Barremian age for bauxite formation on the basis of a reasonable genetic correlation between bauxite deposits and lateritic clays at Roca Vidal which formed on emerged coastal areas of the Ebro massif during the Lower Cretaceous. In this context, bauxites would have formed on coastal plains via the bauxitization of terrigenous sediments supplied from the Ebro massif to the N and the pristine bauxite horizons would subsequently be eroded, reworked and redeposited in their present positions. In fact, observed breccia textures in conjunction with abundant roundgrains and mm- to cm-sized clastic bauxite fragments with highly variable internal textures strongly support an allochthonous origin relative to the karstified area.

Therefore, results of parental rock indices are in line with the observed textural and sedimentary structures, as well as mineralogical observations in the bauxitic samples and the bauxite genesis hypothesis of [47]. They point to an argillaceous sedimentary precursor material supplied by the erosion of igneous rocks of intermediate composition from the now-eroded Ebro massif (paleo-high coinciding with the present-day Ebro basin, source area mainly consisting of Palaeozoic rocks, active from Early Mesozoic until Eocene [69,70]) to the N of the studied bauxite deposits.

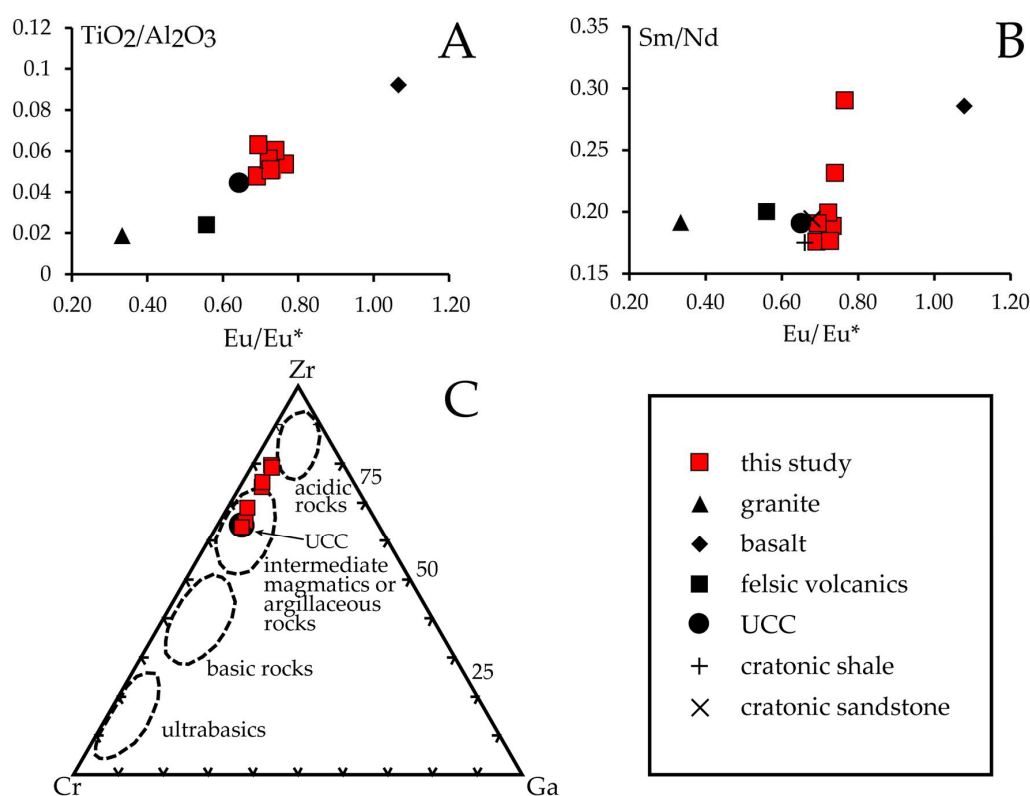


**Figure 11.** (A)  $TiO_2/Al_2O_3$  vs.  $Eu/Eu_N^*$  diagram after [30]. (B)  $Sm/Nd$  vs.  $Eu/Eu_N^*$  diagram after [32]. Note that bauxitic samples from the CCR plot close to values for the Upper Continental Crust (UCC; A,B) and close to values for cratonic sandstone and shale (B). (C) Ternary Zr-Cr-Ga plot after [66]. The samples show acidic to intermediate magmatic/ argillaceous parental affinities.

## 5.2. Mobilization and Fractionation of REE

In spite of the widespread view that REE do not fractionate in supracrustal processes [71–73], some authors suggest that mobilization and fractionation of REE can occur during surface alteration of rocks [61,65,74]. According to Aubert et al. [75] the abundance and leaching behavior of rock-forming and accessory minerals that act as scavengers for REE may be key factors governing the mobilization and fractionation of the REE. Maksimović and Pantó [27] suggest that elements such as the REE, Ni, Co, Mn and Zn in Mediterranean-type karst bauxites can be concentrated in authigenic minerals occurring

in the lowermost part of the deposit, close to the footwall carbonates, where carbonate dissolution creates a buffer system at neutral to slightly alkaline conditions [76,77]. Under these conditions carbonate complexes prevail [78,79]. The resulting alkaline pH barrier is assumed responsible for the precipitation of authigenic minerals from the percolating solutions that infiltrate through the bauxite precursor material during bauxitization [26]. At low pH, REE are readily removed from the weathering profiles, whereas they are fixed by scavengers under neutral or alkaline conditions [61], making the pH one of the key factors controlling the mobilization of REE. During weathering, HREE are preferentially leached since they form aqueous complexes more easily than LREE [80]. The stability of these aqueous complexes increases with increasing atomic number, resulting in a preferential formation of HREE carbonate complexes that are retained in solution, whereas LREE may get adsorbed onto minerals, leading to a LREE enrichment relative to HREE [81,82].

In this study LREE/HREE, as well as  $La_N/Yb_N$ ,  $La_N/Sm_N$  and  $Sm_N/Yb_N$  ratios are used to decipher fractionation between LREE, MREE and HREE. LREE/HREE ratios vary between 4.6 and 10.6 (av. = 8.0), indicating an enrichment of LREE relative to HREE. The highest fractionation tends to occur in the samples with the lowest  $SiO_2$  contents (Table 2). However, there are notable exceptions (samples MI-2, MM-3 and MM-4) so that virtually no predictions regarding the relationship of the degree of REE fractionation and  $SiO_2$  contents can be made.

$La_N/Yb_N$  ratios vary between 4.19 and 10.76 (av. = 8.68) but generally oscillate around 10 (Table 2).  $La_N/Sm_N$  ratios vary between 2.21 and 6.14 (av. = 4.2) which indicates that the enrichment of LREE relative to the MREE is less pronounced than the enrichment of LREE relative to HREE.  $Sm_N/Yb_N$  ratios oscillate between 1.58 and 2.5 (av. = 2.1) which shows only slight fractionation between MREE and HREE.  $La_N/Yb_N$  and LREE/HREE indicate enrichment of LREE relative to HREE by a factor of ~9–10. Enrichment of LREE to MREE is less pronounced with a factor of ~5, as is the enrichment of MREE relative to HREE (by factor ~2). Samples MM-3 and MM-4 show significantly lower values for  $La_N/Yb_N$ ,  $La_N/Sm_N$  and  $Sm_N/Yb_N$  meaning that less fractionation took place during bauxitization. Using chondrite-normalized  $La_N/Yb_N$ - (~10),  $La_N/Sm_N$ - (~4) and  $Sm_N/Yb_N$ - (~2.5) ratios of the Post-Archean Australian Shale (PAAS) as a proxy for the composition of the UCC, it is evident that they are very similar to those observed in the analyzed bauxitic samples. In contrast to karst bauxites of the Parnassos-Ghiona deposits in Greece, the studied bauxitic samples of the CCR do not show positive Ce-anomalies. Gamaletsos et al. [21] showed that the positive Ce-anomalies at Parnassos-Ghiona are high in the uppermost Fe-depleted bauxite domain, but rather low in the lowermost Fe-rich domain. They interpreted these observations as oxidation of  $Ce^{3+} \leftrightarrow Ce^{4+}$  and remobilization of LREE during diagenetic or supergene/epigenetic processes coupled with a generally downward movement of REE in the bauxite profiles. Positive Ce-anomalies in the uppermost parts of bauxite deposits in the Spinazzola area, Italy, are attributed to Ce oxidation and precipitation of cerianite, whereas negative Ce-anomalies prevail in the lower parts of the deposits and close to the footwall carbonates, due to REE scavenging of Ce-depleted percolating solutions by Fe-oxide and precipitation of  $Ce^{3+}$  as fluorocarbonate minerals, respectively [29]. However, in most of the bauxite deposits displayed in Figure 4B there are no Ce-anomalies visible, as is the case for the studied bauxites of the CCR. The lack of positive Ce-anomalies in these bauxites indicates that Ce oxidation did not take place during bauxitization. In contrast to bauxite deposits of Parnassos-Ghiona [21], Ce-anomalies cannot be used as tracers for diagenetic or supergene/epigenetic processes in our study case.

However, observed  $La_N/Yb_N$  variations might indicate pH fluctuations of the percolating waters over time and between different sampling sites. The sustained presence of hematite implies neutral to slightly alkaline conditions in a later stage of bauxite formation. The presence of REE-bearing phosphate minerals likewise suggests near-neutral to slightly alkaline formation conditions and  $[CO_3^{2-}/PO_4^{3-}] < 20$  [83]. Provided that the pH dropped significantly, weathering of primary phosphates (e.g., apatite-, monazite- and allanite-group minerals) may release significant amounts of REE that have the potential to largely dominate REE signatures and budgets of soils, even if initial contents are low [84]. If phosphate ions prevail, they may have the potential to trap dissolved REE

in secondary phosphates (e.g., florencite-, rhabdophane- and xenotime-group). However, secondary phosphate minerals tend to disappear in highly weathered material, meaning that control of the REE distribution by phosphates is constrained to early stages of weathering of precursor materials with elevated phosphate contents [84]. In the light of the present study, this implies that the bauxite precursor material probably had an important sedimentary component and contained elevated initial phosphorus contents. Moreover, the presence of both primary and secondary phosphate minerals suggests that bauxitization stopped before all these mineral grains were leached and totally removed. This would also explain the elevated SiO<sub>2</sub> contents and eventually point to an incomplete bauxitization. Similar values of chondrite-normalized La<sub>N</sub>/Yb<sub>N</sub>, La<sub>N</sub>/Sm<sub>N</sub> and Sm<sub>N</sub>/Yb<sub>N</sub> ratios of the PAAS [85] and the analyzed bauxitic samples indicate that bauxite formation did not lead to significant REE fractionation. Rather, the REE distribution pattern of the CCR bauxites was governed by the REE budget of the bauxite precursor material. Still, this does not foreclose REE remobilization and precipitation of authigenic REE-phases during bauxitization. REE remobilization, as shown by the presence of authigenic REE phases, required acidic conditions, whereas REE entrapment took place under near-neutral to alkaline conditions. The latter is supported by the presence of calcite and hematite in the bauxitic samples.

### 5.3. Minerals Controlling REE Distribution

According to Laveuf and Cornu [84], some secondary minerals, such as Fe- and Mn-oxides or hydroxides, phosphates, clay minerals, as well as certain rock-forming mineral relicts, such as zircon, garnet or titanite are the main sinks of REE. Moreover, important scavengers, preferentially fixing mobile REE, such as Fe-hydroxides (e.g., goethite) forming ooids, have been reported in Italian karst bauxites [29–31]. Apart from the afore-mentioned minerals the contents of REE and their corresponding fractionation might equally be controlled by the presence of rare earth minerals [29,30]. In order to identify mineral phases that control the distribution of REE attempts have been made to correlate REE contents with selected major element oxides, minor and trace elements. No correlation exists between  $\Sigma$ REE and Al<sub>2</sub>O<sub>3</sub>, SiO<sub>2</sub>, TiO<sub>2</sub> or MnO ( $R^2 < 0.2$ ), indicating that REE are unlikely to be bound/adsorbed to clay minerals, Al-oxyhydroxides, Ti-oxides or Mn-oxyhydroxides. Comparison of  $\Sigma$ REE with Fe<sub>2</sub>O<sub>3</sub> reveals a fair negative correlation ( $R^2 \sim 0.5$ ), suggesting that Fe-oxides formed via processes incompatible with the enrichment of REE. Therefore, scavenging effects of Fe- and Mn-oxides or hydroxides, as observed in Italian karst bauxite deposits, are not confirmed for the bauxitic ores of the CCR. The lack of correlation between  $\Sigma$ REE and Al<sub>2</sub>O<sub>3</sub> and SiO<sub>2</sub> is reflected in the fact that EPMA analysis did not reveal elevated REE contents in the kaolin mineral-rich matrix. Hence, REE enrichment via the adsorption on clay mineral surfaces is ruled out for bauxites from the CCR at this stage of investigation.

In contrast, the observed positive correlation between  $\Sigma$ REE with P<sub>2</sub>O<sub>5</sub> ( $R^2 \sim 0.4$ ) (Figure 3J) supports the mineralogical observations described here since only REE-bearing phosphates, namely monazite-(Ce) and xenotime-(Y), (and no carbonates) of mostly detrital origin have been detected in the studied bauxitic samples. Hence, it is assumed that REE are predominantly concentrated in detrital phosphate minerals. Textural evidence (e.g., irregular grain morphologies, concentric growth textures, intergrowth of grains with the kaolin mineral-rich matrix, alteration rim of a detrital xenotime-grain) of unidentified REE-phosphate phases in thin section might indicate that a small fraction of the REE budget of the sampled bauxites is hosted by authigenic phosphate phases.

Both monazite and xenotime are known to incorporate the penalty elements Th and U up to several wt %. Maximum contents of ThO<sub>2</sub> and UO<sub>2</sub> can be as high as 27 wt % and 0.8 wt % in monazite and 8.4 wt % and 5.8 wt % in xenotime [2]. Maksimović and Pantó [27] presented ThO<sub>2</sub> contents  $\leq 0.8$  wt % for authigenic monazite-(La) from the Liverovici bauxite deposit, Montenegro, whereas [20] reported ThO<sub>2</sub>  $\leq 3.6$  wt % for residual monazite-(Ce) from the Zagrad bauxite deposit, Montenegro. Average ThO<sub>2</sub> contents in monazite and xenotime from bauxitic samples of the CCR are 2.33 wt % and 0.18 wt %, respectively. Average UO<sub>2</sub> contents for monazite and xenotime are 0.09 wt % and 0.49 wt %, respectively. In the light of these data average ThO<sub>2</sub> and UO<sub>2</sub> contents of monazite

and xenotime from bauxitic samples of the CCR lie well within the established limits. The average ThO<sub>2</sub> content of monazite is also comparable to ThO<sub>2</sub> contents of detrital monazite-(Ce) of the Zagrad bauxite deposit in Montenegro.

Although several authors cite REE-bearing fluorocarbonates of the bastnäsite group as the most common authigenic rare earth minerals in karst bauxites [27,29,32,86,87], Gamaletsos et al. [21] described a much more varied REE mineralogy for bauxite deposits of the Parnassos-Ghiona area in Greece. These authors reported authigenic LREE<sup>3+</sup> fluorocarbonates (bastnäsite/ parisite-group) as the most abundant REE-phases along with minor LREE oxides, florencite, rhabdophane, xenotime, churchite, monazite, cerianite, as well as kaolinite-associated authigenic REE-phases. Furthermore, there are known examples of karst bauxites with a phosphate-dominated REE mineralogy, e.g., karst bauxites in the Sierra de Bahoruco, Dominican Republic [88] or the Zagrad deposit, Nikšić area, Montenegro [20]. Moreover, Maksimović and Pantó [27] described authigenic monazite-(La) and monazite-(Nd) in the Marmara deposit, Greece and the Liverovici deposit, Montenegro. Based on their phosphate-dominated REE mineralogy karst bauxites from the CCR might be grouped into the latter category.

## 6. Conclusions

On the basis of the application of mineralogical and geochemical analytical methods to bauxitic samples from the Catalan Coastal Range, NE-Spain, we conclude that:

- The most likely precursor material of the bauxitic rocks were argillaceous sediments, possibly derived from igneous rocks of intermediate composition during the erosion of the Ebro massif paleo-high.
- The main REE-minerals are monazite-(Ce) and xenotime-(Y) of detrital origin. Unidentified REE-phosphate grains show textural evidence that may point to an authigenic origin.
- Leaching of the REE probably took place under acidic conditions, whereas the crystallization of rare earth minerals required near neutral to alkaline (pH 6–10) and overall oxidizing conditions during an incomplete bauxitization process.
- Adsorption on Fe- and Mn-oxyhydroxides and clay minerals can be ruled out as a REE scavenging mechanism in the bauxitic ores of the CCR.
- The absence of REE-bearing carbonates and the presence of phosphates as the only REE-bearing mineral phases indicates distinctly different formation conditions than in other Mediterranean-type karst bauxites and suggests relatively high initial phosphorus contents.

**Author Contributions:** J.A.P. conceived the ideas for this study. J.A.P., C.V.-d.-B., L.T., T.B.-A. and R.S. collected the samples and provided the field information. N.R. prepared the samples, performed the analyses, interpreted the data and wrote the paper. T.B.-A. revised and improved the petrographic description. J.A.P., T.A., C.V.-d.-B. and L.T. provided support in the data interpretation. The manuscript was revised by J.A.P., R.S., T.B.-A., T.A. L.T., C.V.-d.-B. and A.D.

**Funding:** This study was partially financed by the Caribbean Lithosphere Research Group (<http://caribbeanlithos.com/>) and the department of Mineralogy, Petrology and Applied Geology of the University of Barcelona. The RWTH Aachen University is thanked for providing financial support (Erasmus + Traineeship grant).

**Acknowledgments:** We want to thank three anonymous reviewers for their criticism that greatly improved our manuscript.

**Conflicts of Interest:** The authors declare no conflict of interest.

## References

1. Wall, F. Rare earth elements. In *Critical Metals Handbook*; Gunn, G., Ed.; John Wiley & Sons: Oxford, UK, 2013; pp. 312–339. ISBN 978-1-118-75534-1.
2. Chakhmouradian, A.R.; Wall, F. Rare Earth Elements: Minerals, Mines, Magnets (and More). *Elements* **2012**, *8*, 333–340. [[CrossRef](#)]

3. Goldschmidt, V.M.; Barth, T.; Lunde, G. *Geochemische Verteilungsgesetze der Elemente. 5, Isomorphie und Polymorphie der Sesquioxide. Die Lanthaniden-Kontraktion und ihre Konsequenzen*; Jacob Dybwad: Oslo, Norway, 1925. (In German)
4. Goodenough, K.M.; Wall, F.; Merriman, D. The Rare Earth Elements: Demand, Global Resources, and Challenges for Resourcing Future Generations. *Nat. Resour. Res.* **2018**, *27*, 201–216. [[CrossRef](#)]
5. Dutta, T.; Kim, K.-H.; Uchimiya, M.; Kwon, E.E.; Jeon, B.-H.; Deep, A.; Yun, S.-T. Global demand for rare earth resources and strategies for green mining. *Environ. Res.* **2016**, *150*, 182–190. [[CrossRef](#)] [[PubMed](#)]
6. Binnemans, K.; Jones, P.T.; Müller, T.; Yurramendi, L. Rare Earths and the Balance Problem: How to Deal with Changing Markets? *J. Sustain. Metall.* **2018**, *4*, 126–146. [[CrossRef](#)]
7. Binnemans, K.; Jones, P.T. Rare Earths and the Balance Problem. *J. Sustain. Metall.* **2015**, *1*, 29–38. [[CrossRef](#)]
8. Directorate-General for Internal Market, Industry, Entrepreneurship and SMEs, European Commission; Deloitte Sustainability; British Geological Survey. *Toegepast Natuurwetenschappelijk Onderzoek Study on the Review of the List of Critical Raw Materials Final Report*; European Commission: Brussels, Belgium, 2017; ISBN 978-92-79-47937-3.
9. Goodenough, K.M.; Schilling, J.; Jonsson, E.; Kalvig, P.; Charles, N.; Tuduri, J.; Deady, E.A.; Sadeghi, M.; Schiellerup, H.; Müller, A.; et al. Europe's rare earth element resource potential: An overview of REE metallogenetic provinces and their geodynamic setting. *Ore Geol. Rev.* **2016**, *72*, 838–856. [[CrossRef](#)]
10. Mordberg, L.E. Patterns of distribution and behaviour of trace elements in bauxites. *Chem. Geol.* **1993**, *107*, 241–244. [[CrossRef](#)]
11. Klyucharev, D.S.; Volkova, N.M.; Comyn, M.F. The problems associated with using non-conventional rare-earth minerals. *J. Geochem. Explor.* **2013**, *133*, 138–148. [[CrossRef](#)]
12. Deady, É.; Mouchos, E.; Goodenough, K.; Wall, F. Rare Earth Elements in Karst-Bauxites: A Novel Untapped European Resource? In Proceedings of the European Rare Earth Resources Conference, Milos, Greece, 4–7 September 2014; p. 12.
13. Torró, L.; Proenza, J.A.; Aiglsperger, T.; Bover-Arnal, T.; Villanova-de-Benavent, C.; Rodríguez-García, D.; Ramírez, A.; Rodríguez, J.; Mosquea, L.A.; Salas, R. Geological, geochemical and mineralogical characteristics of REE-bearing Las Mercedes bauxite deposit, Dominican Republic. *Ore Geol. Rev.* **2017**, *89*, 114–131. [[CrossRef](#)]
14. Hind, A.R.; Bhargava, S.K.; Grocott, S.C. The surface chemistry of Bayer process solids: A review. *Colloids Surf. Physicochem. Eng. Asp.* **1999**, *146*, 359–374. [[CrossRef](#)]
15. Deady, É.A.; Mouchos, E.; Goodenough, K.; Williamson, B.J.; Wall, F. A review of the potential for rare-earth element resources from European red muds: Examples from Seydişehir, Turkey and Parnassus-Giona, Greece. *Mineral. Mag.* **2016**, *80*, 43–61. [[CrossRef](#)]
16. Borra, C.R.; Pontikes, Y.; Binnemans, K.; Van Gerven, T. Leaching of rare earths from bauxite residue (red mud). *Miner. Eng.* **2015**, *76*, 20–27. [[CrossRef](#)]
17. Borra, C.R.; Mermans, J.; Blanpain, B.; Pontikes, Y.; Binnemans, K.; Van Gerven, T. Selective recovery of rare earths from bauxite residue by combination of sulfation, roasting and leaching. *Miner. Eng.* **2016**, *92*, 151–159. [[CrossRef](#)]
18. Vind, J.; Malfliet, A.; Blanpain, B.; Tsakiridis, P.; Tkaczyk, A.; Vassiliadou, V.; Pantias, D. Rare Earth Element Phases in Bauxite Residue. *Minerals* **2018**, *8*, 77. [[CrossRef](#)]
19. Aiglsperger, T.; Proenza, J.A.; Lewis, J.F.; Labrador, M.; Svojtka, M.; Rojas-Purón, A.; Longo, F.; Ďurišová, J. Critical metals (REE, Sc, PGE) in Ni laterites from Cuba and the Dominican Republic. *Ore Geol. Rev.* **2016**, *73*, 127–147. [[CrossRef](#)]
20. Radusinović, S.; Jelenković, R.; Pačevski, A.; Simić, V.; Božović, D.; Holclajtner-Antunović, I.; Životić, D. Content and mode of occurrences of rare earth elements in the Zagrad karstic bauxite deposit (Nikšić area, Montenegro). *Ore Geol. Rev.* **2017**, *80*, 406–428. [[CrossRef](#)]
21. Gamaletsos, P.N.; Godelitsas, A.; Filippidis, A.; Pontikes, Y. The Rare Earth Elements Potential of Greek Bauxite Active Mines in the Light of a Sustainable REE Demand. *J. Sustain. Metall.* **2018**. [[CrossRef](#)]
22. Bárdossy, G. *Karst Bauxites: Bauxite Deposits on Carbonate Rocks*; Developments in Economic Geology; Distribution for the U.S.A. and Canada, Elsevier Science Pub. Co: Amsterdam, The Netherlands; New York, NY, USA, 1982; ISBN 978-0-444-99727-2.

23. Bárdossy, G.; Aleva, G.J.J. *Lateritic Bauxites*; Developments in Economic Geology; Distribution for the U.S.A. and Canada, Elsevier Science Pub. Co: Amsterdam, The Netherlands; New York, NY, USA, 1990; ISBN 978-0-444-98811-9.
24. Mordberg, L.E.; Stanley, C.J.; Germann, K. Mineralogy and geochemistry of trace elements in bauxites: The Devonian Schugorsk deposit, Russia. *Mineral. Mag.* **2001**, *65*, 81–101. [[CrossRef](#)]
25. Wang, X.; Jiao, Y.; Du, Y.; Ling, W.; Wu, L.; Cui, T.; Zhou, Q.; Jin, Z.; Lei, Z.; Weng, S. REE mobility and Ce anomaly in bauxite deposit of WZD area, Northern Guizhou, China. *J. Geochem. Explor.* **2013**, *133*, 103–117. [[CrossRef](#)]
26. Maksimović, Z.; Pantó, G. Contribution to the geochemistry of the rare earth elements in the karst-bauxite deposits of Yugoslavia and Greece. *Geoderma* **1991**, *51*, 93–109. [[CrossRef](#)]
27. Maksimović, Z.; Pantó, G. Authigenic rare earth minerals in karst-bauxites and karstic nickel deposits. In *Rare Earth Minerals: Chemistry, Origin, and Ore Deposits*; Jones, A.P., Ed.; Mineralogical Society Series; Chapman & Hall: London, UK, 1996; pp. 257–279. ISBN 978-0-412-61030-1.
28. Ochsenkühn-Petropulu, M.; Ochsenkühn, K.M. Rare earth minerals found in Greek bauxites by scanning electron microscopy and electron probe micro-analysis. *Microsc. Anal.* **1995**, *37*, 33–34.
29. Mongelli, G. Ce-anomalies in the textural components of Upper Cretaceous karst bauxites from the Apulian carbonate platform (southern Italy). *Chem. Geol.* **1997**, *140*, 69–79. [[CrossRef](#)]
30. Marni, P.; Mongelli, G.; Oggiano, G.; Dinelli, E. Geological, geochemical and mineralogical features of some bauxite deposits from Nurra (Western Sardinia, Italy): Insights on conditions of formation and parental affinity. *Int. J. Earth Sci.* **2007**, *96*, 887–902. [[CrossRef](#)]
31. Boni, M.; Rollinson, G.; Mondillo, N.; Balassone, G.; Santoro, L. Quantitative Mineralogical Characterization of Karst Bauxite Deposits in the Southern Apennines, Italy. *Econ. Geol.* **2013**, *108*, 813–833. [[CrossRef](#)]
32. Mongelli, G.; Boni, M.; Buccione, R.; Sinisi, R. Geochemistry of the Apulian karst bauxites (southern Italy): Chemical fractionation and parental affinities. *Ore Geol. Rev.* **2014**, *63*, 9–21. [[CrossRef](#)]
33. Putzolu, F.; Piccolo Papa, A.; Mondillo, N.; Boni, M.; Balassone, G.; Mormone, A. Geochemical Characterization of Bauxite Deposits from the Abruzzi Mining District (Italy). *Minerals* **2018**, *8*, 298. [[CrossRef](#)]
34. Haniç, N. Geological and geochemical evolution of the Bolkardağı bauxite deposits, Karaman, Turkey: Transformation from shale to bauxite. *J. Geochem. Explor.* **2013**, *133*, 118–137. [[CrossRef](#)]
35. Maksimović, Z.; Pantó, G. Hydroxyl-bastnaesite-(Nd), a new mineral from Montenegro, Yugoslavia. *Mineral. Mag.* **1985**, *49*, 717–720. [[CrossRef](#)]
36. Molina, J.M. A review of karst bauxites and related paleokarsts in Spain. *Acta Geol. Hung.* **1991**, *34*, 179–194.
37. Salas, R.; Vaquer, R.; Travé, A. Bauxitas kársticas y arcillas lateríticas berremienses de la Cadena Ibérica oriental y la Cadena Costera Catalana: Relaciones genéticas y áreas de procedencia. *Geo-Temas* **2004**, *6*, 4. (In Spanish)
38. Ordóñez, S.; Fort, R.; Bustillo, M. Estudio de las tierras raras en las bauxitas karsticas del noreste de la península ibérica. *Estud. Geol.* **1990**, *46*, 373–384. (In Spanish) [[CrossRef](#)]
39. Yuste, A.; Bauluz, B.; Mayayo, M.J. Genesis and mineral transformations in Lower Cretaceous karst bauxites (NE Spain): Climatic influence and superimposed processes: Lower Cretaceous Karst Bauxites. *Geol. J.* **2015**, *50*, 839–857. [[CrossRef](#)]
40. Yuste, A.; Bauluz, B.; Mayayo, M.J. Origin and geochemical evolution from ferrallitized clays to karst bauxite: An example from the Lower Cretaceous of NE Spain. *Ore Geol. Rev.* **2017**, *84*, 67–79. [[CrossRef](#)]
41. Guimerà, J. Palaeogene evolution of deformation in the northeastern Iberian Peninsula. *Geol. Mag.* **1984**, *121*, 413. [[CrossRef](#)]
42. Guimerà, J.; De Vicente, G.; Rodríguez Pascua, M.A.; Muñoz Martín, A.; Vegas, R.; Simón, J.L. Cadenas con cobertura: Las cadenas Ibérica y Costera Catalana. In *Geología de España*; Vera, J.A., Ed.; Sociedad Geológica de España: Salamanca, Spain; Ministerio de Educación y Ciencia, Instituto Geológico y Minero de España: Madrid, Spain, 2004; pp. 602–617. ISBN 978-84-7840-546-6. (In Spanish)
43. Catalunya, I.C. i G. de ICGC—Vissir3. Available online: <http://www.icc.cat/vissir3/> (accessed on 18 September 2017).
44. Salas, R.; Querol, X.; Fernandez Turriel, J.L.; Lopez Soler, A. *The Bauxite and Lateritic Clay Deposits of NE Spain*; University of Barcelona: Barcelona, Spain, 1990.

45. Anadón, P.; Colombo, F.; Esteban, M.; Marzo, M.; Robles, S.; Santanach, P.; Solé Sugrañés, Y.L. Evolución tectonoestratigráfica de los Catalánides. *Acta Geol. Hispànica* **1979**, *242–270*.
46. Salas, R.; Guimerà, J.; Mas, R.; Martín-Closas, C.; Meléndez, A.; Alonso, A. Evolution of the Mesozoic central Iberian rift system and its Cainozoic inversion (Iberian Chain). In *Peri-Tethyan Rift/Wrench Basins and Passive Margins*; Ziegler, P.A., Ed.; Peri-Tethys Memoir; Publications Scientifiques du Muséum: Paris, France, 2001; pp. 145–185. ISBN 978-2-85653-528-8.
47. Combes, P.J. *Recherches sur la genèse des bauxites dans le Nord-Est de l’Espagne, le Languedoc et l’Ariège (France)*; Foundation C.E.R.G.A.: Montpellier, France, 1969. (In French)
48. Anadón, P.; Cabrera, L.; Guimerà, J.; Santanach, P. Paleogene Strike-Slip Deformation and Sedimentation Along the Southeastern Margin of the Ebro Basin. In *Strike-Slip Deformation, Basin Formation, and Sedimentation*; Biddle, K.T., Christie-Blick, N., Eds.; SEPM Society for Sedimentary Geology: Broken Arrow, OK, USA, 1985; pp. 303–318.
49. Universitat de Barcelona Hydroseparation Laboratory Barcelona. Available online: <http://hslab-barcelona.com/> (accessed on 26 September 2018).
50. Cabri, L.J.; Rudashevsky, N.S.; Rudashevsky, V.N.; Oberthür, T. Electric-Pulse Disaggregation (Epd), Hydroseparation (Hs) and Their Use in Combination for Mineral Processing and Advanced Characterization of Ores. In Proceedings of the 40th Annual Canadian Mineral Processors Conference, Ottawa, ON, Canada, 22–24 January 2008; pp. 211–235.
51. Aiglsperger, T.; Proenza, J.A.; Zaccarini, F.; Lewis, J.F.; Garuti, G.; Labrador, M.; Longo, F. Platinum group minerals (PGM) in the Falcondo Ni-laterite deposit, Loma Caribe peridotite (Dominican Republic). *Miner. Depos.* **2015**, *50*, 105–123. [[CrossRef](#)]
52. Mongelli, G.; Boni, M.; Oggiano, G.; Mameli, P.; Sinisi, R.; Buccione, R.; Mondillo, N. Critical metals distribution in Tethyan karst bauxite: The cretaceous Italian ores. *Ore Geol. Rev.* **2017**, *86*, 526–536. [[CrossRef](#)]
53. Bau, M.; Dulski, P. Distribution of yttrium and rare-earth elements in the Penge and Kuruman iron-formations, Transvaal Supergroup, South Africa. *Precambrian Res.* **1996**, *79*, 37–55. [[CrossRef](#)]
54. McDonough, W.F.; Sun, S.-S. The composition of the Earth. *Chem. Geol.* **1995**, *120*, 223–253. [[CrossRef](#)]
55. Whitney, D.L.; Evans, B.W. Abbreviations for names of rock-forming minerals. *Am. Mineral.* **2010**, *95*, 185–187. [[CrossRef](#)]
56. Lafuente, B.; Downs, R.T.; Yang, H.; Stone, N. The power of databases: The RRUFF project. In *Highlights in Mineralogical Crystallography*; Armbruster, T., Danisi, R.M., Eds.; DE GRUYTER: Berlin, Germany; München, Germany; Boston, MA, USA, 2015; pp. 1–30, ISBN 978-3-11-041710-4.
57. Lenz, C.; Nasdala, L.; Talla, D.; Hauzenberger, C.; Seitz, R.; Kolitsch, U. Laser-induced REE<sup>3+</sup> photoluminescence of selected accessory minerals—An “advantageous artefact” in Raman spectroscopy. *Chem. Geol.* **2015**, *415*, 1–16. [[CrossRef](#)]
58. MacLean, W.H.; Bonavia, F.F.; Sanna, G. Argillite debris converted to bauxite during karst weathering: Evidence from immobile element geochemistry at the Olmedo Deposit, Sardinia. *Miner. Deposita* **1997**, *32*, 607–616. [[CrossRef](#)]
59. Lyew-Ayee, P.A. A case for the volcanic origin of Jamaican bauxites. In Proceedings of the Bauxite Symposium VI, Kingston, Jamaica, March 1986; p. 30.
60. Pye, K. Bauxites gathering dust. *Nature* **1988**, *333*, 800–801. [[CrossRef](#)]
61. Nesbitt, H.W. Mobility and fractionation of rare earth elements during weathering of a granodiorite. *Nature* **1979**, *279*, 206–210. [[CrossRef](#)]
62. Gamaletsos, P.N.; Godelitsas, A.; Kasama, T.; Church, N.S.; Douvalis, A.P.; Göttlicher, J.; Steininger, R.; Boubnov, A.; Pontikes, Y.; Tzamos, E.; et al. Nano-mineralogy and -geochemistry of high-grade diasporic karst-type bauxite from Parnassos-Ghiona mines, Greece. *Ore Geol. Rev.* **2017**, *84*, 228–244. [[CrossRef](#)]
63. Gamaletsos, P.; Godelitsas, A.; Mertzimekis, T.J.; Göttlicher, J.; Steininger, R.; Xanthos, S.; Berndt, J.; Klemme, S.; Kuzmin, A.; Bárdossy, G. Thorium partitioning in Greek industrial bauxite investigated by synchrotron radiation and laser-ablation techniques. *Nucl. Instrum. Methods Phys. Res. Sect. B Beam Interact. Mater. Atoms* **2011**, *269*, 3067–3073. [[CrossRef](#)]
64. Ahmadnejad, F.; Zamanian, H.; Taghipour, B.; Zarasvandi, A.; Buccione, R.; Salamab Ellahi, S. Mineralogical and geochemical evolution of the Bidgol bauxite deposit, Zagros Mountain Belt, Iran: Implications for ore genesis, rare earth elements fractionation and parental affinity. *Ore Geol. Rev.* **2017**, *86*, 755–783. [[CrossRef](#)]

65. Mongelli, G. REE and other trace elements in a granitic weathering profile from “Serre”, southern Italy. *Chem. Geol.* **1993**, *103*, 17–25. [[CrossRef](#)]
66. Özlü, N. Trace-element content of “Karst Bauxites” and their parent rocks in the mediterranean belt. *Miner. Depos.* **1983**, *18*, 469–476. [[CrossRef](#)]
67. MacLean, W.H.; Kranidiotis, P. Immobile elements as monitors of mass transfer in hydrothermal alteration; Phelps Dodge massive sulfide deposit, Matagami, Quebec. *Econ. Geol.* **1987**, *82*, 951–962. [[CrossRef](#)]
68. Mindszenty, A. The lithology of some Hungarian bauxites—A contribution to the palaeogeographic reconstruction. *Acta Geol. Acad. Sci. Hung.* **1984**, *27*, 441–455.
69. Misch, P.H. *Der Bau der mittleren Südpirenen: Mit 6 Taf. u. 51 Abb. im Text*; Weidmann: Berlin, Germany, 1934. (In German)
70. Ashauer, H.; Teichmüller, R. *Die Variscische und Alpidische Gebirgsbildung Kataloniens; mit 7 Tafeln und 48 Textabbildungen*; Weidmann: Berlin, Germany, 1935. (In German)
71. Wildeman, T.E.; Condie, K.C. Rare earths in Archean graywackes from Wyoming and from the Fig Tree Group, South Africa. *Geochim. Cosmochim. Acta* **1973**, *37*, 439–453. [[CrossRef](#)]
72. Nance, W.B.; Taylor, S.R. Rare earth element patterns and crustal evolution—II. Archean sedimentary rocks from Kalgoorlie, Australia. *Geochim. Cosmochim. Acta* **1977**, *41*, 225–231. [[CrossRef](#)]
73. Muzaffer Karadağ, M.; Küpeli, Ş.; Arýk, F.; Ayhan, A.; Zedef, V.; Döyen, A. Rare earth element (REE) geochemistry and genetic implications of the Mortaş bauxite deposit (Seydişehir/Konya–Southern Turkey). *Chem. Erde Geochem.* **2009**, *69*, 143–159. [[CrossRef](#)]
74. Duddy, L.R. Redistribution and fractionation of rare-earth and other elements in a weathering profile. *Chem. Geol.* **1980**, *30*, 363–381. [[CrossRef](#)]
75. Aubert, D.; Stille, P.; Probst, A. REE fractionation during granite weathering and removal by waters and suspended loads: Sr and Nd isotopic evidence. *Geochim. Cosmochim. Acta* **2001**, *65*, 387–406. [[CrossRef](#)]
76. Fritz, B.; Tardy, Y. Etude thermodynamique du système gibbsite, quartz, kaolinite, gaz carbonique. Application à la genèse des podzols et des bauxites. *Sci. Géol. Bull.* **1973**, *26*, 339–367. [[CrossRef](#)]
77. Drever, J.I. *The Geochemistry of Natural Waters*; Prentice Hall: Englewood Cliffs, UK, 1988; ISBN 978-0-13-351396-7.
78. Johannesson, K.H.; Lyons, W.B.; Stetzenbach, K.J.; Byrne, R.H. The solubility control of rare earth elements in natural terrestrial waters and the significance of  $\text{PO}_4^{3-}$  and  $\text{CO}_3^{2-}$  in limiting dissolved rare earth concentrations: A review of recent information. *Aquat. Geochem.* **1995**, *1*, 157–173. [[CrossRef](#)]
79. Johannesson, K.H.; Stetzenbach, K.J.; Hodge, V.F.; Berry Lyons, W. Rare earth element complexation behavior in circumneutral pH groundwaters: Assessing the role of carbonate and phosphate ions. *Earth Planet. Sci. Lett.* **1996**, *139*, 305–319. [[CrossRef](#)]
80. Mao, J.; Lehmann, B.; Du, A.; Zhang, G.; Ma, D.; Wang, Y.; Zeng, M.; Kerrich, R. Re-Os Dating of Polymetallic Ni-Mo-PGE-Au Mineralization in Lower Cambrian Black Shales of South China and Its Geologic Significance. *Econ. Geol.* **2002**, *97*, 1051–1061. [[CrossRef](#)]
81. Sholkovitz, E.R. The aquatic chemistry of rare earth elements in rivers and estuaries. *Aquat. Geochem.* **1995**, *1*, 1–34. [[CrossRef](#)]
82. Pourret, O.; Gruau, G.; Dia, A.; Davranche, M.; Molénat, J. Colloidal Control on the Distribution of Rare Earth Elements in Shallow Groundwaters. *Aquat. Geochem.* **2010**, *16*, 31–59. [[CrossRef](#)]
83. Morán, D.A. Caracterización y Estabilidad de Carbonatos de Elementos de Tierras Raras en Bauxitas Kársticas. Master’s Thesis, University of Barcelona, Barcelona, Spain, 2017. (In Spanish)
84. Laveuf, C.; Cornu, S. A review on the potentiality of Rare Earth Elements to trace pedogenetic processes. *Geoderma* **2009**, *154*, 1–12. [[CrossRef](#)]
85. Pourmand, A.; Dauphas, N.; Ireland, T.J. A novel extraction chromatography and MC-ICP-MS technique for rapid analysis of REE, Sc and Y: Revising CI-chondrite and Post-Archean Australian Shale (PAAS) abundances. *Chem. Geol.* **2012**, *291*, 38–54. [[CrossRef](#)]
86. Liu, X.; Wang, Q.; Zhang, Q.; Zhang, Y.; Li, Y. Genesis of REE minerals in the karstic bauxite in western Guangxi, China, and its constraints on the deposit formation conditions. *Ore Geol. Rev.* **2016**, *75*, 100–115. [[CrossRef](#)]



87. Berger, A.; Janots, E.; Gnos, E.; Frei, R.; Bernier, F. Rare earth element mineralogy and geochemistry in a laterite profile from Madagascar. *Appl. Geochem.* **2014**, *41*, 218–228. [[CrossRef](#)]
88. Proenza, J.A.; Aiglsperger, T.; Villanova-de-Benavent, C.; Torró, L.; Rodríguez, D.; Ramírez, A.; Rodríguez, J. Discovery of REE minerals hosted in karst bauxite ores from the Sierra de Bahoruco, Pedernales, Dominican Republic. In Proceedings of the 14th SGA Biennial Meeting, Québec City, QC, Canada, 20–23 August 2017; Volume 4, p. 5.



© 2018 by the authors. Licensee MDPI, Basel, Switzerland. This article is an open access article distributed under the terms and conditions of the Creative Commons Attribution (CC BY) license (<http://creativecommons.org/licenses/by/4.0/>).